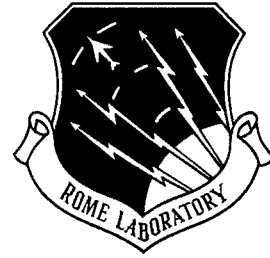


RL-TR-97-180
Interim Report
October 1997



GLOBAL CLUTTER MODEL FOR HF RADARS

SRI International

Roland T. Tsunoda

APPROVED FOR PUBLIC RELEASE; DISTRIBUTION UNLIMITED.


DTIC QUALITY INSPECTED 4

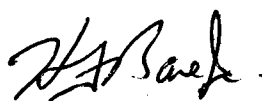
**Rome Laboratory
Air Force Materiel Command
Rome, New York**

19980505 076

This report has been reviewed by the Rome Laboratory Public Affairs Office (PA) and is releasable to the National Technical Information Service (NTIS). At NTIS it will be releasable to the general public, including foreign nations.

RL-TR-97-180 has been reviewed and is approved for publication.

APPROVED: 
ELIHU J. TICHOVOLSKY
Project Engineer

FOR THE DIRECTOR: 
HAROLD F. BARE, JR., Lt Col, USAF
Deputy Director
Electromagnetics & Reliability Directorate

If your address has changed or if you wish to be removed from the Rome Laboratory mailing list, or if the addressee is no longer employed by your organization, please notify RL/ERCE, 31 Grenier St., Hanscom AFB MA 01731-3010. This will assist us in maintaining a current mailing list.

Do not return copies of this report unless contractual obligations or notices on a specific document require that it be returned.

REPORT DOCUMENTATION PAGE			Form Approved OMB No. 0704-0188	
Public reporting burden for this collection of information is estimated to average 1 hour per response, including the time for reviewing instructions, searching existing data sources, gathering and maintaining the data needed, and completing and reviewing the collection of information. Send comments regarding this burden estimate or any other aspect of this collection of information, including suggestions for reducing this burden, to Washington Headquarters Services, Directorate for Information Operations and Reports, 1215 Jefferson Davis Highway, Suite 1204, Arlington, VA 22202-4302, and to the Office of Management and Budget, Paperwork Reduction Project (0704-0188), Washington, DC 20503.				
1. AGENCY USE ONLY (Leave blank)		2. REPORT DATE Oct 97		3. REPORT TYPE AND DATES COVERED Interim Jul 91 - Nov 92
4. TITLE AND SUBTITLE GLOBAL CLUTTER MODEL FOR HF RADARS			5. FUNDING NUMBERS C - F19628-91-K-0008 PE - 62702F PR - 4600 TA - 16 WU - 35	
6. AUTHOR(S) Roland T. Tsunoda				
7. PERFORMING ORGANIZATION NAME(S) AND ADDRESS(ES) SRI International 333 Ravenswood Ave. Menlo Park, CA 94025-3493			8. PERFORMING ORGANIZATION REPORT NUMBER SRI Project 2359	
9. SPONSORING/MONITORING AGENCY NAME(S) AND ADDRESS(ES) Rome Laboratory/ERCP 31 Grenier St. Hanscom AFB, MA 01731-3010			10. SPONSORING/MONITORING AGENCY REPORT NUMBER RL-TR-97-180	
11. SUPPLEMENTARY NOTES Rome Laboratory Project Engineer: Eli Tichovolsky, ERCE, 617-377-2900				
12a. DISTRIBUTION AVAILABILITY STATEMENT Approved for public release; distribution unlimited.			12b. DISTRIBUTION CODE N/A	
13. ABSTRACT (Maximum 200 words) Over-the-Horizon radars (OTHR) operating in the high frequency (HF) band are challenged by spread-Doppler clutter and blanketing sporadic E. Magnetic field-aligned irregularities imbedded in nighttime E layers are identified as a new source component of spread-Doppler clutter. In particular, observations of very high frequency (VHF) spread-Doppler signatures are explained in terms of a polarization electric field model which is applicable to HF as well. In addition, the seasonal morphology of sporadic E occurrence is explained in terms of the ionospheric electric field, which acts as the controlling factor over the metallic ion supply. Knowledge of this electric field will allow prediction of sporadic E occurrences.				
14. SUBJECT TERMS Over-the-Horizon Radar, Sporadic E, spread-Doppler clutter, Magnetic Field-Aligned Irregularities, Gradient-Drift Instability Acoustic Gravity Waves			15. NUMBER OF PAGES 92	
			16. PRICE CODE	
17. SECURITY CLASSIFICATION OF REPORT UNCLASSIFIED	18. SECURITY CLASSIFICATION OF THIS PAGE UNCLASSIFIED	19. SECURITY CLASSIFICATION OF ABSTRACT UNCLASSIFIED	20. LIMITATION OF ABSTRACT UL	

CONTENTS

	CONTENTS.....	i
	LIST OF ILLUSTRATIONS.....	ii
	EXECUTIVE SUMMARY	iv
1	INTRODUCTION.....	1
1.1	Project Objective and Approach.....	1
1.2	Overview of Research Activity	1
1.3	Organization of Report.....	2
2	SPREAD-DOPPLER CLUTTER FROM FIELD-ALIGNED IRREGULARITIES IN SPORADIC E	3
2.1	Introduction	3
2.2	Summary of Observations.....	6
2.3	An Altitude-Modulated E_s Model.....	12
2.4	Discussion and Conclusions	32
3	SPORADIC- E MODELING.....	36
3.1	Introduction	36
3.2	Review of E_s	38
3.3	Ion Transport Equations.....	44
3.4	Electric Field Control.....	55
3.5	Discussion and Conclusions	67
4	DISCUSSION AND FUTURE DIRECTION	69
	REFERENCES.....	71

LIST OF ILLUSTRATIONS

Figure

1	Spread-Doppler clutter characteristics associated with magnetic-aspect-sensitive backscatter from mid-latitude sporadic E	3
2	The backscatter geometry in the elevation plane for beam 3 of the MU radar which is directed toward true north.....	8
3	Example of a single quasi-periodic echo with a negative range-rate that extends from >125 km altitude down to 95 km.....	9
4	Altitude profiles for the spatial wavelengths of primary waves that can excite 3.2 m secondary plasma waves for $V_d = 50, 100, 200, 300$ m/s	17
5	Pedersen conductances for an E_S layer as a function of its position in altitude ...	24
6	Schematic drawing of an AGW-modulated E_S sheet and associated electrodynamics.....	25
7	The polarization electric field computed for two amplitudes of altitude modulation	26
8	Model of a tilted FAI sheet model to explain negative range-rate	29
9	Range rates as a function of FAI sheet propagation direction for different tilt angles	31
10	Occurrence frequency (percent) of intense E_S ($f_o E_S \geq 10$ MHz) observed over Kokubunji, Japan, 1958-1966; reproduced from <i>Smith</i> [1968]	39
11	Diurnal variation in the occurrence of intense E_S ($f_o E_S \geq 10$ MHz) at three ionosonde stations: Kokubunji, Wakkanai, and Ft. Belvoir, reproduced from <i>Smith</i> [1968].....	39

12	Long-term occurrence of E_S at Kokubunji, Japan over eight consecutive years (reproduced from <i>Kasuya</i> [1958]).....	41
13	Schematic drawing of an E_S layer situated at an east-west node of a left circularly polarized, tidal wind profile.....	47
14	Vector orientation of the ionospheric electric field that produces convergent ion motion in the E region.....	53
15	Hodographs of electron drift velocity plotted as function of local time for (a) spring, (b) summer, (c) autumn, and (d) winter over Shigaraki, Japan; averaged solar activity conditions.....	56
16	Circulation of metallic ions as a function of altitude and local time produced by the summer electric-field pattern in Figure 15(b).....	58
17	Circulation of metallic ions as a function of altitude and local time produced by the winter electric-field pattern in Figure 15(d).....	59
18	Circulation of metallic ions as a function of altitude and local time produced by the spring electric-field pattern in Figure 15(a).....	62
19	Circulation of metallic ions as a function of altitude and local time produced by the autumn electric-field pattern in Figure 15(c).....	63
20	Hodographs of electron drift velocity during the summer, for high and low solar activity conditions.	64
21	Circulation of metallic ions as a function of altitude and local time produced by the summer electric-field pattern under high solar-activity conditions.....	65
22	Circulation of metallic ions as a function of altitude and local time produced by the summer electric-field pattern under low solar-activity conditions.....	66
23	Hodograph of electron drift velocity during winter, for high and low solar activity conditions.....	67

EXECUTIVE SUMMARY

Radars that operate in the high-frequency (HF) band, i.e., 3 to 30 MHz, continue to play strategic roles in government service; e.g., over-the-horizon radars (OTHR) are currently being applied to the drug interdiction problem. While HF radars like the OTHR are capable of providing unsurpassed surveillance capabilities, their performance can be severely degraded by ionospheric propagation effects. Propagation effects that continue to cause debilitating problems include various forms of radar clutter, especially those that fall under the category called spread-Doppler clutter, and blanketing sporadic E (E_s) layers that impose reductions and ambiguities in the surveillance-area coverage. Because OTHR participation in strategic missions is crucial to their success but at the same time very expensive, there is good reason to conduct a research program directed toward the reduction and mitigation of these propagation effects.

The objective of this project is to dedicate that kind of technical effort. The basic approach is to apply our continually growing knowledge of ionospheric and plasma physics to the practical problems encountered by operational systems. While we do not recommend this approach for all problems, we believe that this is often the only cost-effective approach available to us for crucial problems on which progress toward solutions has stagnated for lack of an adequate data base or understanding. Topics that fall within this category of problems include the above-mentioned spread-Doppler clutter and those associated with E_s . To remain within the scope of project funding, we have conducted focused investigations on specific problems whose solutions are intended to be useful in the development of functional modules for a global clutter model for HF radars. Topic selection has been guided by problems that appear to be of most concern (as expressed by the OTHR community) and by those most amenable to useful solution.

During the first half of this contract, we investigated two topics: (1) a new form of spread-Doppler clutter produced by irregularities imbedded in nighttime E_s layers, and (2) the seasonal morphology of E_s occurrence. The first topic was considered important because this type of radar echo, recently described by *Yamamoto et al.* [1991], represents a component of spread-Doppler clutter that has not yet been identified as such nor characterized for the OTHR community. Identification and characterization of all constituents that contribute to what is called spread-Doppler clutter are necessary steps toward proper interpretation and eventual mitigation. This particular form of clutter, for

example, could be of considerable interest to the drug interdiction problem because it occurs at night, at mid-latitudes, and often appears as discrete targets in range with sustained movement toward the probing radar. With their associated broad Doppler spectra, these echoes might also appear as false targets imbedded in spread-Doppler clutter.

The second topic was selected, after discussions with the technical monitor on this project, because E_s is a phenomenon that has remained one of the foremost obstacles to effective OTHR performance and one that continues to perplex researchers. It was our impression that general understanding of the E_s process must be grossly lacking when well-accepted wind-shear theory fails completely to explain the observations of a distinctive seasonal behavior, i.e., the daytime summer maximum in E_s occurrence [e.g., *Whitehead*, 1970; 1989]. From our viewpoint, this distinctive seasonal morphology contained a strong clue to the identity of an as yet unnamed physical parameter that must be controlling E_s occurrence. With the new knowledge that has accumulated through basic research in the fields of atmospheric and ionospheric physics, the time seemed opportune for hypothesis testing. With success, we held hope that our findings could be used to develop a truly predictive model for E_s , not one based simply on data-limited statistics. The results from our investigations on these two topics are summarized in the following paragraphs.

The newly identified component of spread-Doppler clutter occurs in mid-latitude E_s layers at night with backscatter confined to directions orthogonal to the geomagnetic field (\vec{B}). The backscatter is produced by field-aligned irregularities in electron density that result from a plasma instability acting on one side of an E_s layer. This form of clutter, which has not been appreciated until recently, differs from that attributed to meteor scatter. Doppler spreading in a meteor echo is caused by its transient appearance in time. Clutter from meteor echoes, therefore, is comprised of random occurrences of a number of impulsive bursts. The clutter described here persists for up to an hour during which a single echo could last for minutes while moving steadily toward the radar; or the clutter could appear as a train of echoes with a quasi-period of several minutes. Another difference is that while meteor activity is known to maximize near dawn, these quasi-periodic (QP) echoes favor the pre-midnight period.

Using data collected with the 46.5 MHz MU radar in Japan (because of its high spatial and temporal resolution), we have determined that these QP echoes have range

versus time characteristics that resemble those associated with atmospheric gravity waves (AGW). Their Doppler characteristics indicate the presence of an electric field (\vec{E}) that is larger than expected in the ambient ionosphere. Adapting the altitude-modulated E_s model proposed by *Woodman et al.* [1991], we have shown, for the first time, that a large-scale polarization \vec{E} develops as a result of the altitude modulation imposed by an AGW on the originally flat E_s layer. The polarization \vec{E} then adds to the ambient background \vec{E} to produce the large observed electric field.. The broad Doppler spreading can then be interpreted as a consequence of two-dimensional mixing of plasma waves [e.g., *Sudan et al.*, 1973] and backscatter associated with those secondary waves. Our polarization model, therefore, is consistent with observations and accounts for the relatively long-lived spread-Doppler clutter.

Besides identifying the source of the broad Doppler spectra, we have shown why these QP echoes move almost always inward (toward the radar) in range. In our model, a passing AGW modulates the E_s layer in altitude. Because the most efficient geometry for this modulation process is one in which an AGW propagates with an equatorward component and with its phase fronts aligned with the \vec{B} , the tilt of the E_s sheet would be downward in the plane of the propagation vector. We show that with this geometry, horizontal movement of the modulated E_s sheet through the radar beam produces (in most cases) an inward movement in range of the intersection point; this represents the discrete QP echo.

On our second topic, we believe we have made a breakthrough in our understanding of the physics that controls E_s occurrence. A well-founded premise has been that wind shears are responsible for E_s formation when there is a supply of metallic ions available. Because wind shears do not display the distinctive seasonal pattern found in E_s occurrence, one must find a process or parameter that controls the supply of metallic ions to the E region. Unfortunately, trace ion constituents in the ionosphere cannot be easily detected; consequently, there continues to exist a paucity of knowledge on the distribution and circulation of metallic ions in the ionosphere. Our principal finding is that we have identified the ionospheric \vec{E} as that controlling parameter of metallic ion supply..

To demonstrate the control of metallic-ion supply by \vec{E} , we used recently reported measurements of \vec{E} by the MU incoherent-scatter radar in Japan [*Oliver et al.*, 1993] and

calculated the circulation patterns of metallic ions in altitude as a function of local time. We showed that the ion circulation has a seasonal pattern and that these patterns are consistent with the hypothesis that a metallic-ion supply is readily available during the summer but not other seasons. As further validation, we showed that this circulation pattern is independent of solar activity, a property that is also reflected in the occurrence of E_s .

To summarize, technical effort during the first half of this project has resulted in two major accomplishments on topics that impact OTHR performance. The first is that we have identified a new component of spread-Doppler clutter that can be found at mid-latitudes during the night and have constructed a polarization \vec{E} model that accounts for spread-Doppler signatures. If the model is correct, we will be able to provide new interpretation for OTHR clutter signatures from mid-latitudes. The second is the identification of the ionospheric \vec{E} pattern as the controlling source of the seasonal morphology of E_s occurrence. We validated this hypothesis through the modeling of ion circulation in altitude as a function of local time for different seasons and solar activity conditions. Knowing that \vec{E} controls E_s occurrence, we now have hope of predicting E_s by monitoring \vec{E} . Both findings represent new fundamental results that should prove valuable when applied to OTHR propagation-effects problems.

1 INTRODUCTION

1.1 PROJECT OBJECTIVE AND APPROACH

The broad objective of this project is to devote a level of technical effort toward the development of a global clutter model that can be used to improve the performance of radars that operate in the high-frequency (HF) band, i.e., 3 to 30 MHz. Clutter is defined here as unwanted radar echoes that degrade the performance of such radars. The envisioned global clutter model would eventually contain a collection of modules, each describing the characteristics of a specific kind of clutter. The intent here is not to develop a complete set of modules that addresses all forms of clutter encountered by HF radars. Development of such a comprehensive model is well beyond the scope of the funded program. Instead, effort will be directed toward the development of one or more modules that describe selected forms of clutter. In addition to the clutter problem, we are also concerned with the problems caused by sporadic- E (E_s) layers. The primary role of E_s layers is to disrupt normal sky-wave propagation characteristics and to introduce ambiguities into ray-path descriptions.

The basic approach taken for this project has been to conduct investigations that lead to a working knowledge of the underlying physical processes that produce and control the characteristics of radar clutter and E_s . Because little is yet known about such processes, a large portion of the technical effort has been and will continue to be devoted to basic research. Unlike, for example, our good understanding of auroral E -region clutter [e.g., *Tsunoda et al.*, 1991], there is relatively little known yet about the topics of spread-Doppler clutter and E_s .

1.2 OVERVIEW OF RESEARCH ACTIVITY

Research activity during the period 1 July 1991 to 1 November 1992 was divided into three parts: (1) sporadic E topics, (2) equatorial spread-Doppler clutter topics, and (3) preparation for equatorial spread-Doppler clutter experiments. The diversion of effort from E_s modeling to equatorial clutter investigations was driven by the fact that spread-Doppler clutter represents the single most insidious problem for OTHRs. Rome Laboratory and the OTHR community in general are concerned about spread-Doppler clutter effects on OTHRs, and are interested in collaborating with the Australians under

the joint U.S.-Australia Memorandum of Understanding. The distribution of effort into three areas has led us to focus less on the E_s problem. However, as described in this interim technical report, significant progress has been made in the area of E_s and related clutter effects.

1.3 ORGANIZATION OF REPORT

The results of our work are presented in order of their relative levels of completeness. We present first, in Section 2, our findings of a newly identified source of spread-Doppler clutter in nighttime, mid-latitude E_s layers. We show that this form of clutter, which has likely been associated with meteor echoes, is one of several components that make up what has been called spread-Doppler (or residual) clutter. Its spread spectrum is shown to be produced by the development of a polarization electric field rather than a transient time behavior. We then present, in Section 3, results of our efforts to understand the physical process controlling E_s occurrence. As discussed in that section, simple wind-shear theory has remained incapable of accounting for the seasonal occurrence of E_s . We close the report with a discussion of our findings and the approach we intend to take for the second half of this research project.

2 SPREAD-DOPPLER CLUTTER FROM FIELD-ALIGNED IRREGULARITIES IN MID-LATITUDE SPORADIC E

2.1 INTRODUCTION

In this section, we report our findings about a form of spread-Doppler clutter which occurs at night in association with mid-latitude E_s . These radar echoes are curious because they are discrete in range extent but often have broad Doppler spectra [e.g., Yamamoto *et al.*, 1991]. Examples of broad Doppler spectra associated with these radar returns are presented in Figure 1. These examples were obtained with the 46.5 MHz MU radar in Shigaraki, Japan, a mid-latitude location. The broadest spectral width is seen in

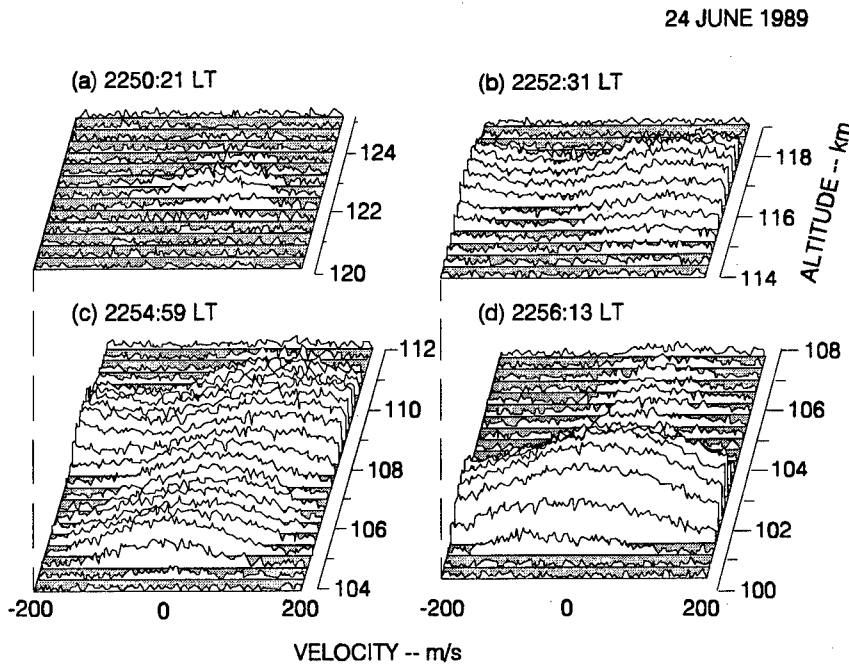


Figure 1 Spread-Doppler clutter characteristics associated with magnetic-aspect-sensitive backscatter from mid-latitude sporadic E

Figure 1(d) to exceed ± 200 m/s and is highly aliased. Unlike spectra from meteor echoes, these broad spectra do not result from impulsive bursts of backscatter; instead, they often persist for minutes and occur in groups with quasi-periodic (QP) characteristics. Because of their curious characteristics and their likely occurrence in the field of view of most OTHRs, we have sought to understand the physical process responsible for their production and, in particular, their broad Doppler spectra. In the following, we describe our findings.

Sporadic- E (E_s) layers in the mid-latitude ionosphere are known to often be associated with field-perpendicular radar backscatter at operating frequencies from 16 to 50 MHz [e.g., *Goodwin and Thomas*, 1963; *Goodwin*, 1965; *Ecklund et al.*, 1981; *Tanaka and Venkateswaran*, 1982a,b; *Keys and Andrews*, 1984; *Riggin et al.*, 1986; *Fukao et al.*, 1991a; *Yamamoto et al.*, 1991, 1992, 1993]. In all cases, researchers have attributed the observed backscatter to field-aligned irregularities (FAI) produced by the gradient-drift instability [e.g., *Simon*, 1963; *Maeda et al.*, 1963; *Tsuda et al.*, 1966; *Kato*, 1972].

Despite an apparent consensus on the basic source mechanism, questions remain as to whether the gradient-drift instability accounts for all of the observed characteristics. One concern has to do with polarization-reducing effects on wave electric fields at mid-latitudes where the geomagnetic field \vec{B} has a finite inclination I . In the simplest case, the electric-potential mapping relation is given by $\lambda_{\perp} \leq \lambda_{\parallel} / \sqrt{\sigma_0 / \sigma_p}$ [*Farley*, 1960], where λ_{\perp} is the perturbation scale size transverse to \vec{B} and λ_{\parallel} is the potential-mapping distance along \vec{B} . The symbols σ_0 and σ_p are the direct and Pedersen conductivities. At E -region altitudes, that relation becomes $\lambda_{\perp} \leq \lambda_{\parallel} / 50$, which means for example that a transverse perturbation in electric potential of 100-m scale size will not map along \vec{B} more than 5 km. *Kato* [1972] obtained identical results, concluding that the gradient-drift instability would be operative only for $\lambda_{\perp} \leq 200$ m. Questions arise, therefore, whenever wavelike variations with $\lambda_{\perp} > 100$ m are attributed to plasma waves generated by the gradient-drift instability.

Interestingly, one of most intriguing features found in field-perpendicular backscatter from mid-latitude E_s layers is a large-scale wavelike variation in mean Doppler velocity and echo power. *Ecklund et al.* [1981] were the first to show that the mean Doppler velocity can vary quasi-periodically with periods of 12 to 15 min and maximum speeds reaching 120 m/s. *Riggin et al.* [1986] later reported wavelike variations in peak Doppler velocity with horizontal wavelengths of 10 to 12 km and periods of 2 to 6 min. While recognizing that these features resembled those of atmospheric gravity waves (AGW), *Riggin et al.* [1986] rejected AGWs as the source because the Doppler velocities were often found to exceed 250 m/s, a speed that is perhaps five times the mean drift speed of the background ionosphere [e.g., *Burnside et al.*, 1983]. For this reason, they chose to interpret these large-scale wavelike variations in terms of kilometer-scale, primary plasma waves generated by the gradient-drift instability. As partial justification, they noted a similarity of these wavelike variations to

those observed in the equatorial electrojet [e.g., *Farley and Balsley, 1973; Kudeki et al. 1982*].

Recently, *Yamamoto et al. [1991, 1992, 1993]* reported high-resolution measurements of field-perpendicular backscatter from E_s using the MU radar. They found that the patterns of echo power when plotted in a range-time-intensity (RTI) format could be categorized into two types, continuous and quasi-periodic (QP), and that the radar range R to each QP echo almost always decreased as a function of time (i.e., a negative range rate). The range rate (\dot{R}) was often found to be nearly constant with speeds of 60 to 90 m/s and not related to the corresponding Doppler velocity. In fact, the Doppler velocity often differed in sign from that of \dot{R} . To explain the occurrence of QP echoes, *Woodman et al. [1991]* suggested that a local treatment of the gradient-drift instability is probably not valid for thin E_s layers. That is, if the opposite walls of an E_s layer are separated by a distance less than the wavelength of the primary plasma wave of interest, an electric field of the perturbation wave would map along \vec{B} from one side of the E_s layer to the other side with virtually no attenuation. In this case, the gradient-drift instability would act to develop oppositely directed, polarization electric fields along the opposite walls and those electric fields would tend to cancel one another. To resolve this problem, *Woodman et al. [1991]* hypothesized that AGWs may be modulating the E_s layers in altitude and causing the directions of the plasma-density gradients to be rotated and more aligned with \vec{B} . They concluded that AGWs with sufficiently large amplitude could produce average gradients that satisfy the field-line-integrated gradient-drift instability for the wavelengths of interest. In this scenario, the striated characteristics of QP echoes would reflect those of the AGW and not those of primary plasma waves as suggested by *Riggin et al. [1986]*.

Both interpretations seem unable to account for all three of the major features: (1) kilometer-scale wavelike variations in the mean Doppler velocity, (2) mean Doppler velocities much greater than the background bulk plasma drift, and (3) quasi-periodic pattern in backscatter power. The plasma-wave interpretation does not account for the polarization-cancelling effects, as pointed out by *Woodman et al. [1991]*. And, neither the interpretation in terms of an AGW-induced modulation of an E_s layer nor that in terms of large-scale plasma waves can account for the existence of large, mean Doppler velocities. In order to gain insight into the physical processes that may account for both kilometer-scale, wavelike variations and large mean Doppler velocities, we have re-examined the altitude-modulated E_s model in search of a large-scale polarization process.

Our results indicate that plasma waves with wavelengths of several kilometers are not needed to generate the FAI responsible for radar backscatter. This finding allows us to consider the kilometer-scale wavelike features in terms of AGW-induced characteristics and frees us from our original concern for polarization-reducing effects at those scales. While the concerns by *Woodman et al.* [1991] regarding cancellation of wave electric fields across thin E_s layers remain valid, we show that the wavelengths of the primary waves of interest are small enough that polarization shorting is not dominant. Our most important finding is that altitude modulation of an E_s layer can indeed lead to charge separation and the development of a polarization electric field (\vec{E}_p). This \vec{E}_p appears to be a capable source mechanism for both the kilometer-scale wavelike features and the enhanced Doppler velocities that have been observed.

We begin in Section 2.2 by summarizing the characteristics of QP echoes that all theories must explain. These characteristics are those extracted primarily from MU radar measurements but they are compared to those obtained by other radar measurements. We follow with a description of our altitude-modulated E_s model and the wave-induced polarization process in Section 2.3. We close this topic with a discussion and conclusions in Section 2.4.

2.2 SUMMARY OF OBSERVATIONS

2.2. MU Radar Backscatter Geometry

The first step is to establish the effective spatial resolution of the MU radar for the measurement of QP echoes. The MU radar has sufficient sensitivity to QP echoes to allow use of effective pulsewidths with a range resolution of 300 to 600 m. With this range resolution, the MU radar is easily capable of resolving the spatial wavelengths of kilometer-scale, wavelike structures that might propagate radially with respect to the radar. On the other hand, angular resolution is of some concern because the illuminated scattering volume is large compared with the expected distribution of FAI in an E_s layer. Fortunately, the size of the echoing region is determined primarily by the magnetic aspect sensitivity of the backscatter. There exists good evidence that E_s backscatter is confined to directions approximately $\pm 0.5^\circ$ about the field-perpendicular direction. For example, *Riggin et al.* [1986] used radar interferometry with a baseline in the north-south direction to obtain measurements consistent with this estimate. *Yamamoto et al.* [1991] showed

that backscatter profiles obtained from different radar viewing directions were most consistent with one another when adjusted more precisely with regard to the magnetic aspect geometry. Consequently, the effective radar beamwidth in elevation is likely to be no more than 1° to 2° for radar azimuths close to the magnetic meridian, regardless of the actual beamwidth in elevation. On the other hand, the visibility of FAI in azimuth is not controlled by magnetic aspect sensitivity, at least near the magnetic meridian. Therefore, azimuthal resolution is determined by the radar azimuthal beamwidth.

For the MU radar, which is located in Shiragaki, Japan (34.9°N , 136.1°E), the radar line-of-sight to orthogonal intersection with \vec{B} at E -region altitudes occurs for example at $R \approx 170$ km and 39° elevation in the direction of geographic (true) north. Its phased-array antenna has a two-way, half-power total beamwidth of 4.5° and 2.3° in elevation and azimuth, respectively. As discussed above, the effective beamwidth in elevation is no more than 2° . The corresponding transverse dimensions of the effective scattering region, therefore, are 7 km in azimuth and 6 km in elevation. Because these dimensions are comparable to the spatial wavelengths of QP echoes, it seems that the MU radar might have difficulty in resolving the characteristics of east-west propagating QP echoing regions. This difficulty can be alleviated through the use of interferometry [e.g., Yamamoto *et al.*, 1993] or possibly through Doppler processing. With the described angular sensitivity and a short pulsewidth, the MU radar is also potentially capable of measuring the thickness of the scattering region. For example, with an effective range resolution of 600 m, a horizontal scattering layer that is 1 km thick would extend over 1.5 km in R . However, if the scattering layer is tilted, the estimate of thickness would remain ambiguous.

The spatial coverage provided by one beam of the MU radar can be determined from Figure 2 which shows the elevation geometry for beam 3, which was directed toward true north for the measurements reported by Yamamoto *et al.* [1991]. The boresight of the beam (dash-dotted line) has an elevation angle of 39° , and corresponds to the radar wave vector (\vec{k}_r) shown in the inset in the upper left corner. The full beamwidth is shown by the stippled region and is plotted as a function of altitude and horizontal distance from the radar. Magnetic aspect sensitivity reduces the effective beamwidth to less than one-half the actual beamwidth. Superimposed on the antenna pattern are curves for constant magnetic-aspect angles (A) and R . It is important to note that field-perpendicular backscatter can be detected at all altitudes in the E region, given

the presence of FAI. The echoes observed at various altitudes, however, would correspond to different ground distances from the radar.

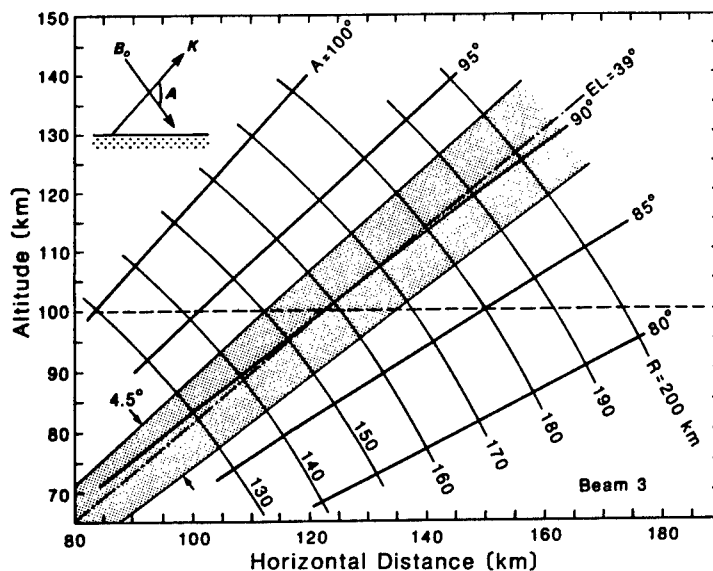


Figure 2 The backscatter geometry in the elevation plane for beam 3 of the MU radar which is directed toward true north.

2.2.2 Characteristics of QP Echoes

Next, we summarize the characteristics of QP echoes that have been extracted from MU radar measurements; most have been reported by *Yamamoto et al.* [1991, 1992, 1993]. These characteristics are referred to throughout this paper by their item numbers.

1. QP echoes always occur at night with preference for the premidnight sector. All other occurrences of field-perpendicular backscatter from E_s have also been at night [e.g., *Ecklund et al.*, 1981; *Tanaka and Venkateswaran*, 1982a, b; *Riggin et al.*, 1986]. Their occurrences have been intermittent and unpredictable. The close association of QP echoes with E_s layers and their nighttime occurrence represent strong evidence that the gradient in plasma density (∇N) is playing an important role in the production of FAI. These gradients associated with convergent layers of metallic ions are masked by the presence of solar-produced ionization during the day.

2. QP echoes occur between 95 and 140 km in altitude (e.g., see *Yamamoto et al.* [1993], their Figure 3). Moreover, they consist of discrete echoes that appear to move coherently over that full altitude interval as a function of time. This coherent movement

appears as downward-sloping striations in RTI plots. The number of striations can vary from 1 to more than 30 in a two-hour period. An example of a striation that extends from 125 km down to 96 km is presented in Figure 3. The striation is seen to have appeared at 125 km altitude around 2250 LT (LT refers to local solar time at 135°E longitude) and to move inward in R as a function of time. Although its intensity varied with altitude (or time), it was continuously visible until its disappearance at 96 km altitude around 2259 LT. *Riggin et al.* [1986] also reported backscatter up to 130 km altitude during the more intense events.

3. The \dot{R} associated with the striations is almost always negative (i.e., inward in range with time) and often nearly constant. The \dot{R} values have been found to vary from -60 to -90 m/s. The \dot{R} also corresponds to altitude descent rates of 40 to 60 m/s. These descent rates are much larger than those associated with tidal modes, e.g., 1.5 m/s [*Fujitaka and Tohmatsu*, 1973], and faster than downward-moving E_s layers associated with AGW motion, e.g., 12 m/s [*Rowe*, 1974].

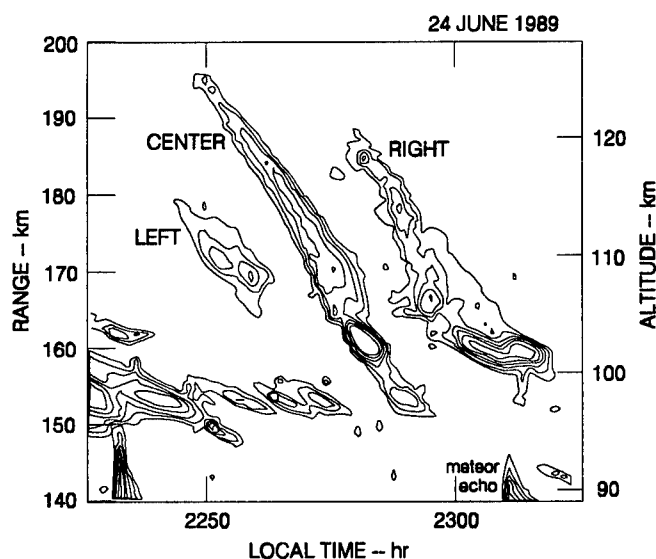


Figure 3 Example of a single QP echo (center striation) with a negative range-rate that extends from >125 km altitude down to 95 km

4. The Doppler velocity characteristics of QP echoes obtained with the MU radar have yet to be analyzed in detail, but preliminary results indicate that the Doppler velocity is unrelated to the corresponding \dot{R} in both magnitude and sign. In contrast to

the often-observed constant \dot{R} , the mean Doppler velocity (for a given altitude and averaged in time) often varied monotonically with altitude, e.g., from +60 m/s at 120 km to -20 m/s at 96 km. That is, there is evidence of an altitude shear in the mean Doppler velocity. The general disparity between Doppler velocity and \dot{R} is strong evidence that \dot{R} is a trace (i.e., apparent) velocity and is not necessarily related to actual irregularity motion.

5. Multi-beam and interferometry measurements have shown that the irregularity drift velocity is usually westward with speeds of 120 to 160 m/s. The westward direction is consistent with the preponderance of westward drifts reported by *Tanaka and Venkateswaran* [1982a]; their reported velocities of 60 to 80 m/s, however, were about a factor of 2 smaller than those obtained with the MU radar. The MU radar results are, however, still smaller than the mean Doppler velocities >250 m/s reported by *Riggin et al.* [1986].

6. QP echoes have periods that range from 2 to 10 min, and striation spacings (in range) at a fixed time of 5 to 15 km. In comparison, *Ecklund et al.* [1981] reported quasi-periods of 12 to 15 min; and *Riggin et al.* [1986] reported periods of 2 to 6 min, and apparent horizontal wavelengths of 10 to 12 km. The range rate, periods and striation spacings are consistent with parameter values that describe AGW propagation.

7. Multi-beam and interferometer measurements have shown unambiguously that westward propagation is accompanied by a tilt whose normal vector has a downward component, which is consistent with AGW characteristics.

8. Stronger echoes often occur at preferred altitudes. The impression that one gets after perusing the MU radar data is that the preferred altitudes are usually below 110 to 115 km. *Woodman et al.* [1991] suggested that the strongest echoes probably occur from altitudes where the E_s layers were located.

9. Backscatter has been detected, from multi-beam measurements, to occur simultaneously over a 64° azimuth sector with a center around 15° east of Magnetic North. The azimuthal sector of backscatter occurrence is either a measure of the angular spectrum of secondary plasma waves (interpreted in terms of the gradient-drift instability) or possibly a measure of the geographical extent of the E_s layer.

2.2.3 Some Preliminary Implications

Striations in RTI plots with $\dot{R} < 0$ could be interpreted in several ways, but we can use the characteristics of QP echoes to eliminate those interpretations that involve quasi-point targets. One interpretation is in terms of a quasi-point target that moves radially toward the radar along the boresight of the antenna; we discard it on the basis that the geometry is physically too restricting. A quasi-point target with a purely downward or purely horizontal motion toward the radar would also produce $\dot{R} < 0$. In these cases, however, the observed range extent of the striations would be limited by the effective beamwidths. It is easily shown that motions of quasi-point targets cannot produce striations that extend from 95 to 140 km in altitude. A horizontally stratified E_s sheet containing FAI and descending in altitude would also produce a trace with $\dot{R} < 0$. Difficulties with this interpretation are: (1) the observed \dot{R} values are too large to correspond with E_s layers descending at nodes of tidal motion; (2) the occurrence of multiple striations, as many as 30 during a two-hour period, seems to contradict the ion-convergence theory for E_s layers and the availability of metallic ions.

The most promising interpretation, therefore, seems to be in terms of a discrete echo that is a tracer for a tilted FAI sheet as it passes through the antenna beam. (This geometry is examined in more detail in Section 2.3.5 and shown to be consistent with the observed values of \dot{R} and the ubiquitous presence of $\dot{R} < 0$.) The MU radar measurements, however, would be ambiguous regarding the angle of spatial tilt of the FAI layer and its direction of propagation. While an equatorward traveling AGW seems capable of accounting for the observations [Yamamoto *et al.*, 1993], questions remain regarding proper interpretation of the MU radar measurements and the generality of the AGW-modulation model. More importantly, none of these geometric considerations have, thus far, shed light on the source of the kilometer-scale wavelike variations and large, mean Doppler velocities.

In the following section, we re-examine the altitude-modulated E_s model proposed by Woodman *et al.* [1991] and show that altitude modulation is accompanied by a polarization process that can account for the puzzling radar observations.

2.3 AN ALTITUDE-MODULATED E_s MODEL

The results are presented in five parts. Because of our original concern with polarization-reducing effects acting on kilometer-scale FAI, we begin (Section 2.3.1) with a brief review of nighttime E_s -layer characteristics measured in situ by rockets. From these characteristics and an analysis of the gradient-drift instability (Section 2.3.2), we show that kilometer-scale, primary plasma waves are not required for the production of field-perpendicular radar backscatter detected around 50 MHz. We also find that the cancellation of wave electric fields because of the thinness of E_s layers is not as serious as suggested by *Woodman et al.* [1991]. The wavelengths of the primary waves that are likely to be involved in the production of radar backscatter are shown to be much shorter than the thickness of a typical E_s layer. While these findings seem to negate the need for an altitude-modulated E_s layer to account for QP echoes, we show that it plays a crucial role in the development of a polarization electric field, \vec{E}_p , that is essential for the linear gradient-drift instability in the production of backscatter. This requirement for an enhanced drift velocity is consistent with the observations (Items 2, 5, 6, 7, and 9). We proceed then to show (Section 2.3.3) that the nighttime mid-atitude ionosphere (item 1) is susceptible to large-scale polarization effects produced by variations in the field-line-integrated Pedersen conductivity (i.e., conductance), Σ_p , of the E_s layer. We examine (Section 2.3.4) the geometry of the altitude-modulated E_s layer and show that a wavelike \vec{E}_p is set up by this kind of geometry. We close by demonstrating (Section 2.3.5) that the behavior of \dot{R} is consistent with a representation of the FAI trace velocity. We show that a tilted E_s sheet propagating horizontally in different directions can produce the ubiquitous occurrence of negative \dot{R} values (item 3).

2.3.1 Nighttime E_s Characteristics

The nighttime E_s layer has been measured in situ over the years by using sensors aboard rockets [*Smith*, 1966, 1970; *Sagalyn et al.*, 1967; *Smith and Mechtly*, 1972; *Smith and Miller*, 1980]; most were made with 10-m spatial resolution. Most E_s layers were found to have a single peak with a simple shape and a thickness that is usually about 2 km but can be as much as 7 km [e.g., *Sagalyn et al.*, 1967]. The measured peak N values are usually less than 10^5 el/cm³. For example, from three rockets launched during the sunset and premidnight sectors, *Smith* [1966] reported peak N values of 3×10^4 to $1.5 \times$

10^5 el/cm^3 . Some of the E_s layers have multiple peaks [e.g., *Smith and Miller, 1980*], which are thought to result from unstable wind shears.

Observations of nighttime E_s layers also seem to contain evidence of altitude modulation. *Smith* [1966] noted, for example, that the altitude of the nighttime E_s layer often disagrees with the virtual height of E_s measured by ionosondes; the agreement during the day, however, is excellent. This discrepancy must be taken seriously because virtual heights correspond nearly to physical altitudes when the gradient is steep. One possibility is that the ionosonde signal reflects from an oblique angle associated with a tilted E_s sheet. Tilts in E_s layers are, however, not usually found in rocket measurements; i.e., significant altitude differences are not often seen between E_s layers encountered during rocket ascent and descent. Then again, these results differ completely with Arecibo incoherent-scatter measurements that contain clear examples of altitude-modulated E_s layers [*Miller and Smith, 1978*]. This apparent discrepancy, which remains to be investigated, could be a result of the use of preferred rocket trajectories. For example, most of the E_s rockets have been launched from Wallops Island, Virginia. It is conceivable that most tilts were not detected because the rockets were all launched eastward and perhaps because most tilts are in the north-south rather than east-west plane. This conjecture is consistent with the altitude-modulated E_s model presented in Section 2.3.4.

The fact that E_s layers are typically thicker than a kilometer suggests that perturbation electric fields of plasma waves with $\lambda_{\perp} \leq 20 \text{ m}$ will not map from one side of an E_s layer to the other. These wavelengths, which can be thought of as being protected from potential-mapping effects, are extremely short for primary waves as discussed below. This is the reason why *Woodman et al.* [1991] suggested the need to consider field-line-integrated behavior. We alleviate their concern in the next subsection by showing that the primary plasma waves that must be involved in the generation of FAI detected by northward-looking radars need not be much greater than 20 m.

2.3.2 Gradient-Drift Instability

The gradient-drift instability, when described using a local approximation, has a linearized growth rate (γ) with the following vector form [e.g., *Woodman et al., 1991*]

$$\gamma \propto \frac{1}{1+\psi} \vec{k} \cdot \vec{V}_{ei} (\vec{k} \cdot \nabla N \times \vec{B}) \quad (1)$$

where $\psi = \nu_i \nu_e / \Omega_i \Omega_e$, ν_i (ν_e) is the ion-neutral (electron-neutral) collision frequency, Ω_i (Ω_e) is the ion (electron) gyrofrequency, \vec{V}_{ei} is the electron drift velocity relative to the ions, and \vec{k} is the wave vector of the plasma wave. At mid-latitudes where \vec{B} has a finite inclination (I), a horizontally stratified E_s layer has an upward (downward) directed gradient in N with components that are northward (southward) and transverse to \vec{B} . From (1), γ therefore reaches a maximum value (γ_0) when \vec{V}_{ei} is directed toward magnetic west (east) and \vec{k} is parallel to \vec{V}_{ei} . Besides a maximum in γ , plasma waves that propagate horizontally tend to stay in the unstable region and grow until saturation occurs. Waves that are directed transverse to \vec{B} but away from \vec{V}_{ei} are characterized by $\gamma < \gamma_0$ and propagate toward the upper or lower boundaries of the unstable region. For example, if $I = 50^\circ$, the wave-growth distance in an E_s layer that is 1 km thick is 0.8 km; and the corresponding growth time is 4 s for a wave phase velocity of 200 m/s. When \vec{V}_{ei} and \vec{k} are parallel but directed away from the east-west plane, $\gamma < \gamma_0$ because the effective transverse gradient ($\nabla_{\perp} N$) decreases and γ becomes zero when \vec{V}_{ei} is in the north-south plane. In these cases, \vec{k} has a vertical component which indicates these waves would have limited growth times. For these reasons, the strongest primary plasma waves (i.e., waves generated directly by the instability) are expected to develop when both \vec{V}_{ei} and \vec{k} are westward (or eastward) in the presence of horizontally stratified E_s layers. This expectation is consistent with observations (item 5).

As noted by *Sudan et al.* [1973] and others, however, the gradient-drift instability has difficulty in accounting for primary waves in the equatorial electrojet that cause backscatter at radar frequencies as high as 46.5 MHz and in the vertical direction. When similar considerations are given to the mid-latitude case, we find from the expected values of \vec{V}_{ei} and $\nabla_{\perp} N$ in E_s layers that irregularity wavelengths no less than about 5 m can grow. (See results given below.) More importantly, field-perpendicular backscatter from E_s layers is often observed when the radar beam is directed northward, a direction corresponding to the vertical direction in the equatorial case and one in which primary waves cannot develop. Both of these difficulties can be eliminated by invoking the production of secondary plasma waves by the gradient-drift instability as shown by *Sudan et al.* [1973]. They showed that when the amplitude of a primary wave becomes large, the wave electric fields can produce local electron drifts that are comparable to \vec{V}_{ei} , and a local gradient $\nabla_{\perp} n$ (where n is the wave perturbation in N) that can be an order of

magnitude greater than that of the background. The latter condition allows secondary-wave growth at wavelengths of a few meters or less.

If the above scenario can account for radar backscatter from E_s layers, we wish to determine the range of wavelengths of the primary waves (λ_p) that are responsible for the generation of the secondary waves that produce backscatter at the MU radar frequency. We can then apply the potential-mapping formula given in Section 2.1 to predict whether the primary waves of interest would be susceptible to polarization-reducing effects, as hypothesized by *Woodman et al.* [1991]. We are also interested in the dependence of this range of λ_p on altitude. Adopting the formulation for γ used by *Sudan et al.* [1973] and neglecting ion inertia, we solve for λ_p ,

$$\lambda_p \leq \frac{v_i^2 \Omega_e V_{ei} A^2 \lambda_s^2}{4\pi v_e \Omega_i C_s^2 (1+\psi)^2} \quad (2)$$

where A is the relative amplitude of the primary wave and C_s is the ion-acoustic speed. The inequality given by (2) states that all primary waves with a λ_p less than that specified by the right-hand side of (2) are capable of exciting secondary waves with a spatial wavelength of λ_s . Intuitively, we should recognize that $\gamma \propto V_{eff} / L_{eff}$, i.e., the growth rate is specified by the ratio of an effective velocity to an effective gradient scale length. For secondary waves, $V_{eff} \propto V_{ei} A$ and $L_{eff} \propto (A / \lambda_p)^{-1}$. In this sense, (2) can be thought of as a specification for L_{eff} that is required for gradient-drift instability growth. In (2), the parameters that control the upper bound on λ_p are \vec{V}_{ei} and A . If these quantities are small, they require that λ_p be small. As can be seen from (2), larger λ_p values can excite secondary waves at a fixed λ_s when \vec{V}_{ei} and A are larger.

For a lower bound on λ_p , we know from conventional gradient-drift instability theory [e.g., *Fejer et al.*, 1984] that the γ for primary plasma waves increases with λ_p for a given \vec{V}_{ei} and $\nabla_{\perp} N$ for the range of λ_p values of interest. (While recombination loss is assumed to be negligible for metallic ions, other factors such as nonlocal effects should be considered when λ_p becomes even larger.) We can, therefore, solve the growth-rate equation ($\gamma > 0$) for λ_p ,

$$\lambda_p \geq 2\pi \left[\frac{v_e L}{v_i \Omega_e V_{ei}} \left[C_s^2 (1+\psi) - \frac{V_{ei}^2}{(1+\psi)} \right] \right]^{1/2} \quad (3)$$

where $L = (\nabla N / N)^{-1}$ is the gradient scale length. Note that (3) states that primary waves of all λ_p are excited when $\bar{V}_{ei} \geq C_s(1 + \psi)$. When this happens, the two-stream instability is excited and is responsible for the shorter λ_p values. We can now use (2) and (3) to bound the range of λ_p for growing primary waves that would excite secondary waves of a given λ_s . (Similar analyses for radar auroral echoes at a fixed altitude have been presented by *Greenwald* [1974] and *Tsunoda* [1976].)

Two sets of curves obtained by using (2) and (3) for $\lambda_s = 3.2$ m (which corresponds to backscatter at 46.5 MHz) are shown in Figure 4 where λ_p is plotted as a function of altitude for four different values of \bar{V}_{ei} . We have used $B = 0.5$ G (which is appropriate for the location of the MU radar) and assumed for simplicity that only Fe^+ ions are present. We have used the neutral temperature profile from *Jacchia* [1971] to compute C_s by equating electron and ion temperatures to the neutral temperature, and have used profiles for v_i and v_e that have the forms given in *Unwin and Knox* [1968] and values at 105 km altitude identical to *Farley and Balsley* [1973]. The curves from (2) are labeled with A values of 2, 4, 8, and 16 percent, while the curves from (3) are labeled with L values of 100, 200, 500, and 1000 m. The values of λ_p that excite secondary waves are those below curves labeled with A values, and those that are excited directly lie above curves labeled with L values. Therefore, primary waves that can grow and excite secondary waves are those in the area between any pair of A - and L -labeled curves.

We expect typical conditions to correspond to the shaded area between the curves defined by $A = 0.04$ and $L = 500$ m. Observations indicate that these values are realistic. *Itoh et al.* [1975], for example, launched a rocket from Uchinoura, Japan at 2100 LT on 27 August 1973 and measured values of A that ranged from 0.01 to 0.05 for irregularity wavelengths between 4 and 100 m. Their measurements, however, were made under what appears to be weak E_s conditions. Therefore, to expect $A > 0.05$ during more intense E_s conditions seems reasonable. And, as mentioned above, rocket measurements indicate that E_s layers have thicknesses that are one kilometer or more. On the average, therefore, we might expect L to be half the thickness of the E_s layer or less.

From the upper left panel in Figure 4, we see that secondary waves are excited only from 97 to 108 km in altitude when \bar{V}_{ei} is 50 m/s, a velocity that is representative of the bulk motion of the background ionosphere (see next subsection). This result cannot

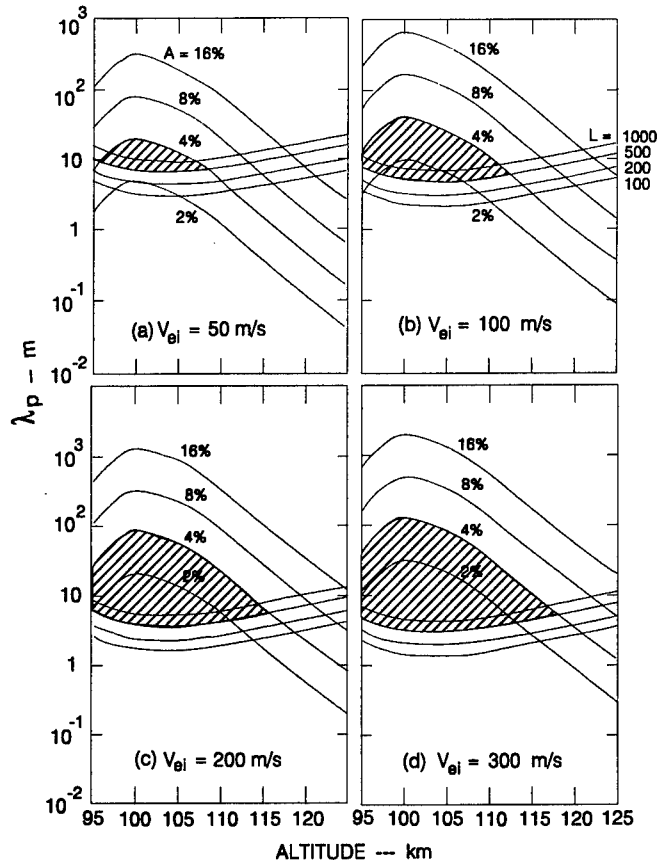


Figure 4 Altitude profiles for the spatial wavelengths of primary waves that can excite 3.2-m secondary plasma waves for $V_d = 50, 100, 200, 300$ m/s.

account for the occurrence of QP echoes up to 140 km altitude (item 2). The altitudes of wave excitation can be increased only slightly even with substantial reduction in L . Larger increases in the wave excitation region can be achieved by increasing A rather than L . Another means of increasing the altitude regime for FAI generation is to increase \vec{V}_{ei} , as shown in the other three panels in Figure 4. When \vec{V}_{ei} becomes 300 m/s, as shown in the lower right panel, secondary waves are generated from well below 95 km to 119 km. (We note that the two-stream instability is excited for \vec{V}_{ei} values on the order of 300 m/s or greater.) While the lower altitude bound for secondary-wave generation is consistent with observations, 119 km is still significantly lower than 140 km. Again, larger values of A would provide better agreement with observations. Computations made using NO^+ ions have shown that the excitation region for secondary waves is even more restricted for lighter ions; therefore, changing the ion composition of the E_s layer does not help.

Another difference between the sets of curves shown in Figure 4 is that the shaded area increases in size with increasing \vec{V}_{ei} . The increase in area results from an increase in the range of λ_p values that are capable of exciting the secondary plasma waves of interest. If we use the potential-mapping relation mentioned in Section 2.1 and discard primary plasma waves with $\lambda_p > 20$ m, we see that the remaining primary plasma waves with shorter scales are entirely capable of producing the secondary waves of interest. Moreover, the range of excitation in altitude is not reduced by the imposed polarization-shortening filter. In fact, meter-scale primary waves are needed for the generation of 3.2-m secondary waves at the higher altitudes. Values of λ_p much smaller than about 30 m must, of course, be interpreted with caution because *Sudan et al.* [1973] assumed that $\lambda_p \gg \lambda_s$. When this approximation is no longer valid, we expect proportionately reduced growth rates. We might expect further reduction in growth rate because these wavelengths are also comparable to the gyroradius for metallic ions, e.g., 2.7 m at 95-km altitude and 4.2 m at 130-km altitude.

The curves in Figure 4, therefore, lead to the following conclusions. If the gradient-drift instability is retained as the sole source mechanism, large values of \vec{V}_{ei} would be necessary for the development of QP echoes. From Figure 4, a \vec{V}_{ei} of 250 m/s and an A of 0.08 or 0.16 are necessary to account the occurrence of QP echoes over extended altitudes (item 2). While 250 m/s is extremely large for drifts found in the mid-latitude ionosphere, this velocity is comparable to the observed Doppler velocities of >250 m/s (item 5). Further agreement with observations can be inferred; for example, if \vec{V}_{ei} is indeed large, secondary waves should be in a state of well-developed, two-dimensional turbulence, which is consistent with item 9. The requirement for \vec{V}_{ei} as large as 250 m/s should not, however, be taken too literally. We should keep in mind that the gradient-drift instability is known to operate at altitudes well into the F region [e.g., *Chiu and Strauss*, 1979]; the difference is that the driver changes from a Hall to a Pedersen current. Although this aspect of the problem remains to be investigated, we should allow for the possibility that the full altitude extent of QP echo occurrence may not have to be accounted for solely by the Hall-current, gradient-drift instability.

The importance of the finding that a large \vec{V}_{ei} value may be required implies the need for a large-scale polarization process to produce enhanced irregularity drifts. We show in Section 2.3.4 that such a process arises naturally in altitude-modulated E_s layers. And, given that \vec{V}_{ei} must be reasonably large, it allows short-scale, primary plasma waves to account for the secondary waves responsible for radar backscatter. If true, the need to

have E_s layers that become aligned with \vec{B} [Woodman *et al.*, 1991] is reduced. Finally, these findings show that the kilometer-scale wavelike features attributed to primary plasma waves by Riggin *et al.* [1986] is not a factor in producing radar backscatter. We are, therefore, free to attribute these wavelike variations to another source, e.g., AGWs.

2.3.3 Altitude-Modulation by an AGW

The concept that a horizontally stratified E_s layer can be modulated in altitude by the passage of an AGW is not new [e.g., From, 1983; Keys and Andrews, 1984; Lanchester *et al.*, 1991; Woodman *et al.*, 1991]. Only Woodman *et al.* [1991], however, have suggested a modulation in E_s that has an amplitude of ± 15 km. We consider the reasonableness of this hypothesis in this section.

In the simplest description of an AGW, its wave vector (\vec{k}_g) is tilted from the horizontal plane by an angle α_g , which is prescribed by the AGW dispersion equation, $\cos \alpha_g = \tau_B / \tau_g$ [e.g., Hines, 1960], where τ_B is the Brunt-Väisälä period and τ_g is the AGW period. For AGWs generated in the lower atmosphere, \vec{k}_g has a downward component. The tilt angle for the planes of constant phase (ϕ_g) for the AGW is simply $90^\circ - \alpha_g$, or $\phi_g = \sin^{-1}(\tau_B / \tau_g)$. In the scenario envisioned by Woodman *et al.* [1991], the AGW propagates southward in the magnetic meridian with ϕ_g equal to I . The motion of the neutral gas produced by the AGW is, therefore, aligned with \vec{B} and efficiently transports ions (through ion drag) to different altitudes. Woodman *et al.* [1991] assumed the vertical transport velocity to be 35 m/s. This velocity is, in fact, comparable to direct estimates of AGW amplitudes [e.g., Whitehead, 1972]. Because the neutral gas moves parallel to \vec{B} , it does not produce a dynamo electric field. Setting $\phi_g = 50^\circ$ and using $\tau_B = 5$ min for E -region altitudes, we have $\tau_g = 6.5$ min which is in the range of the observed periods for the QP echoes and, because the AGW dispersion equation does not specify wavelength (λ_g), Woodman *et al.* [1991] assumed $\lambda_g = 15$ km, as reported by Yamamoto *et al.* [1991]. This set of AGW parameters yields a phase velocity of 38 m/s.

In the scenario proposed by Woodman *et al.* [1991], the applied electric field (\vec{E}_0) is assumed to be directed northward to produce the postulated westward electron drift and, presumably, maximum growth rate for the gradient-drift instability. Given this geometry, we need to consider ion motion, because the formation of an E_s layer requires

the presence of long-lived metallic ions and their distribution is transport dominated. Given a background tidal wind system, which we assume to be circularly polarized in a left-hand sense, wind-shear theory [e.g., *Chimonas and Axford, 1968*] predicts that an E_s layer would form at higher altitudes where there is a shear in the north-south wind component. In this case, the metallic ions would be flowing westward in the E_s layer. At lower altitudes, an E_s layer would form where there is a shear in the east-west wind component and, in this case, the ions would be flowing southward in the E_s layer. Of the two types of E_s layers, those at lower altitudes will have ion motion with an eastward component along the bottomside of the E_s layer. Consequently, \vec{V}_{ei} would be larger and lead to correspondingly larger growth rates. This result is consistent with observations of stronger backscatter at lower altitudes (item 8).

The ion motion in an E_s layer must, therefore, rotate from a westward direction at higher altitudes to a southward direction at lower altitudes as the E_s layer is transported downward by the tidal wind system. Superimposed on this ion motion by the winds is that produced by \vec{E}_0 , which is small and northward at low altitudes and larger and westward at higher altitudes. Therefore, if \vec{E}_0/B is smaller than the neutral wind, we can expect ion motion to be southwestward. That the ion drift is southwestward is important for altitude modulation of an E_s layer by a southward propagating AGW. If the E_s layer did not have a southward drift component, the interaction time between AGW and E_s plasma would be limited; for example, the AGW would move 2.3 km/min relative to the ions and phase reversal would occur after 3.3 min. If we use 35 m/s for the vertical transport velocity, the E_s layer would be displaced only 2.1 km in altitude. A southward component of ion motion is, therefore, necessary if the AGW-induced motion is to transport ions over ± 15 km in altitude from the mean location of the E_s layer. For a vertical transport speed of 35 m/s, 7 min is needed to produce a ± 15 -km displacement. This concept of increasing interaction time by matching velocities is often called spatial resonance [*Whitehead, 1971*]. We, therefore, find that an E_s layer in the specified tidal wind system can be modulated in altitude by a southward propagating AGW.

Altitude modulation is also possible by AGWs with an east-west component in their direction of propagation, but the modulation is likely to be less than that of the above described scenario. If \vec{k}_g is rotated out of the magnetic meridian plane, ϕ_g must increase if the AGW phase fronts are to remain aligned with \vec{B} . Because $\sin \phi_g = \tau_B / \tau_g$, τ_g must decrease from 6.5 min toward 5 min. When $\phi_g = 90^\circ$, which is

required for east-west propagation, the AGW would not have a downward phase component; this implies that the AGW would have to be ducted. If ducting does not occur, the phase front of the AGW cannot be aligned with \vec{B} and the effectiveness of the AGW for altitude modulation would be reduced. AGWs propagating with a northward component clearly cannot have phase fronts parallel to \vec{B} ; altitude modulation, therefore, is most difficult for this case. There is also the requirement that λ_g is long enough so that phase reversal does not take place at E -region altitudes. For example, if we set the vertical half-wavelength to be 30 km, $\lambda_g \approx 72$ km, which is 3 to 4 times longer than that found for southward propagation. While these geometries will have to be analyzed in more detail to better understand their characteristics, large-amplitude altitude modulation of E_s layers by AGWs seems to be a reasonable concept.

Before presenting our most interesting finding, the development of a wavelike, polarization electric field with altitude modulation of an E_s layer, we briefly review the nature of \vec{E}_0 in the mid-latitude ionosphere. The behavior of \vec{E}_0 can not only affect the altitude modulation process itself but it also determines the strength of the total electric field that would be observed. At night, \vec{E}_0 is most likely generated by the F -region dynamo [Rishbeth, 1971]. As shown below, the Pedersen conductance (Σ_p) of the nighttime F layer is always greater than that of the nighttime E layer, which is a measure of the relative contributions from dynamo action in the E and F layers. Evidence for control of nighttime ionospheric electrodynamics by the F -region dynamo have been presented, e.g., by Behnke and Hagfors [1974] and Burnside *et al.* [1983].

For our purposes, we have examined the behavior of \vec{E}_0 as measured by the MU radar [Fukao *et al.*, 1991b; Oliver *et al.*, 1993]. During the summer under low solar-activity conditions (using data from 1986 to 1988), the zonal component of plasma drift is eastward from 1700 LT with a maximum speed of 30 m/s occurring around 1830 LT. From 2000 LT, it turns westward and reaches a maximum speed of 25 m/s around 2200 LT. At midnight, the zonal component reverses again and reaches a maximum of 10 m/s around 0200 LT. And at 0300 LT, it becomes westward once again reaching a maximum of 35 m/s around 0630 LT. During the same season under high solar-activity conditions (using data from 1989 to 1991), the behavior of the zonal component is qualitatively the same as that under low solar activity. One difference is that there appears to be a 10 m/s eastward bias in speed. That is, the primary eastward maximum which occurs around 1930 LT is 40 m/s, the westward maximum which occurs around 2300 LT is about 5 m/s, and the secondary eastward maximum is 15 m/s. The other difference is that the

westward maximum which occurs around 0600 LT is 45 m/s, 10 m/s greater than during solar minimum conditions.

The meridional drift component during solar minimum conditions is southward from 1400 LT until 0200 LT; a maximum of 20 m/s is reached around 1830 LT although the speed remains around 15 m/s thereafter. The northward drift lasts only for an hour with a maximum of about 5 m/s. The meridional component becomes southward again, reaching a maximum of 20 m/s around 0430 LT before decreasing toward zero around 0630 LT. During solar maximum conditions, the meridional component also appears to have a 10 m/s southward bias, with maximum speeds of nearly 30 m/s. The other difference is that the post-midnight reversal to a northward drift seen under solar minimum conditions appears to shift to the pre-midnight period, occurring between 1930 and 2200 LT. The maximum northward speed is 10 m/s.

These results provide some idea of the average electrodynamic conditions during the summer months when QP echoes are observed with the MU radar. The westward drift that appears at night is consistent with the preponderance of westward Doppler and irregularity drifts that have been reported (item 5), and the southward drift is consistent with our hypothesis that spatial resonance must play an important role in the altitude modulation process. The central problem, therefore, is to account for the wavelike variations in Doppler velocity whose peak values are larger by a factor of 2 to 5 when compared with the averaged \vec{V}_e for the nighttime ionosphere [Fukao *et al.*, 1991b; Oliver *et al.*, 1993] and by a factor of slightly more than 2 when compared to peak \vec{V}_e that have been measured [e.g., Behnke and Hagfors, 1974; Burnside *et al.*, 1983].

2.3.4 Polarization Produced by Altitude Modulation

Given that an E_s layer can be strongly modulated in altitude (e.g., from 95 to >125 km), we consider whether the redistribution of metallic ions may be accompanied by polarization effects. Polarization (i.e., charge separation) at spatial scales greater than a few kilometers and temporal scales of a few minutes usually occurs as a result of like variations in the Pedersen conductance (Σ_p) and the need by nature to sustain divergence-free currents. For our problem, the variations in the Σ_p of the E_s layer ($\Sigma_p^{E_s}$) must be significant in the presence of an otherwise unchanging Σ_p of the background ionosphere. The strength of the \vec{E}_p that would develop is given by

$$\bar{E}_p = \bar{E}_p^0 \frac{\Sigma_p^{E_s}}{\Sigma_p^{E_s} + \Sigma_p^E + \Sigma_p^F} \quad (4)$$

where \bar{E}_p^0 is the polarization electric field that would develop in the absence of any background conducting layers and Σ_p^E and Σ_p^F refer to Σ_p for the E and F layers, respectively. The second term in (4), i.e., the ratio of Σ_p values, is simply a charge leakage (or polarization-shorting) factor that allows electric charges to neutralize through current closure in different layers. The procedure, therefore, is to first evaluate the Σ_p values in (4) and then to show how \bar{E}_p^0 can develop. In the following, we are only concerned with rough estimates of Σ_p values and, consequently, we have not bothered to give the altitude bounds that should be used to compute Σ_p for each region.

Estimates of Σ_p for the background ionosphere have been obtained with the Arecibo incoherent-scatter radar, both for solar minimum conditions [Harper and Walker, 1977] and for solar maximum conditions [Burnside et al., 1983]. We are interested in the field-line-integrated values; therefore, we have simply divided their measurements of the height-integrated Pedersen conductivities by $\cos I$ where I is 50° at Arecibo. During solar minimum conditions, Σ_p^E varied only slightly during the night, from 0.2 mho at 2030 AST (Atlantic Standard time) to 0.1 mho at 0330 AST. Correspondingly, Σ_p^F varied slightly more, from 0.5 mho at 2030 AST to a minimum value of 0.2 mho at 2330 AST, before increasing slightly to 0.3 mho at later times. During solar maximum conditions, however, Σ_p^F was 8 times larger than during solar minimum conditions, while Σ_p^E remained essentially unchanged. The total Σ_p of the background ionosphere, therefore, varies from as little as 0.3 mho to as much as 2.6 mhos.

For comparison, we estimate Σ_p for an E_s layer that is 1-km thick and composed entirely of metallic Fe^+ ions. Curves of $\Sigma_p^{E_s}$ for N values of 10^3 to 10^6 el/cm³ are plotted as a function of E_s -layer altitude in Figure 5; $\Sigma_p^{E_s}$ varies from 2×10^{-5} mho to slightly greater than 1 mho. We, therefore, find that when N reaches values between 10^5 to 10^6 el/cm³, $\Sigma_p^{E_s}$ is comparable to that of the background ionosphere. Substituting these values of Σ_p in (4), we find that $\bar{E}_p \approx 0.5\bar{E}_p^0$. Rigglin et al. [1986], in fact, reported that on the three nights when field-perpendicular backscatter was detected during simultaneous measurements by the Arecibo incoherent-scatter radar, peak N in the E_s

layers were no less than 2×10^5 el/cm³. These measurements correspond with $\Sigma_p^{E_s}$ values that are greater than 0.4 mho (at 125 km) during occurrences of QP echoes, which is again significant compared to Σ_p for the background ionosphere. The variation in $\Sigma_p^{E_s}$ that results when an E_s layer is modulated in altitude can be determined from Figure 5. For $N = 2 \times 10^5$ el/cm³, $\Sigma_p^{E_s}$ varies from 0.004 mho at 95-km altitude to 0.4 mho at 125 km. We, therefore, conclude that an altitude-modulated E_s layer is capable of supporting a polarization process.

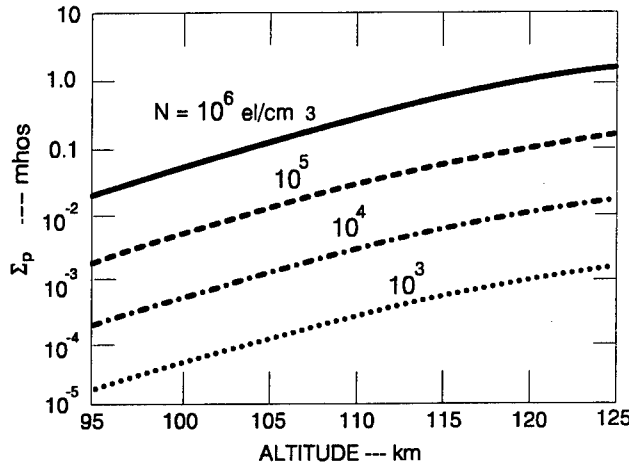


Figure 5 Pedersen conductances for an E_s layer as a function of its position in altitude.

Consider now the electrodynamics of an E_s layer modulated in altitude by a southward-propagating AGW. The process is schematically illustrated in Figure 6. We assume that the phase fronts of the AGW are aligned with I (i.e., $\vec{k}_g \perp \vec{B}$) and that the interaction leads to an altitude-modulated E_s layer, which is represented by the distorted sinusoid drawn with a heavy line in Figure 6. Altitude and northward ground distance in the magnetic meridian are given in Cartesian coordinates. The inclined straight lines are aligned with \vec{B} and shown for $I = 50^\circ$. The variation in the altitude of the E_s layer as a function of distance transverse to \vec{B} translates into a corresponding variation in $\Sigma_p^{E_s}$. This variation resembles a quasi-sinusoid when plotted using a logarithmic scale, which is schematically shown by the solid-line curve in the lower right section of the diagram in Figure 6. The \vec{E}_0 produced by the F -region dynamo is assumed to be directed northward. Because of \vec{E}_0 , the diagram in Figure 6 is in the moving frame drifting westward with a speed of \vec{E}_0/B .

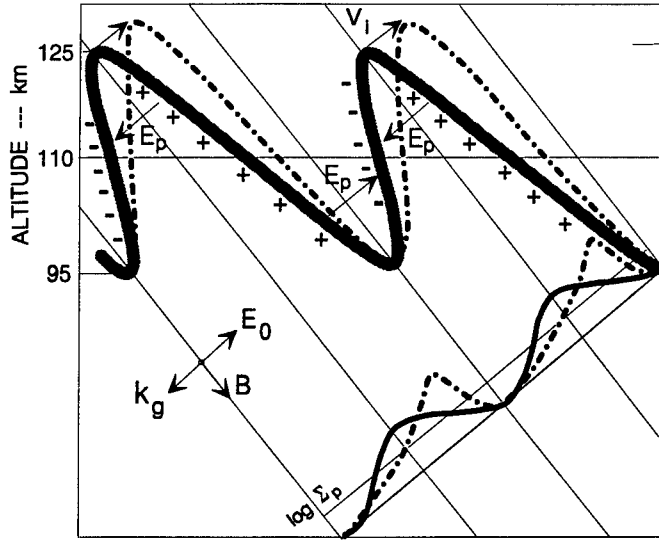


Figure 6 Schematic drawing of an AGW-modulated E_s sheet and associated electrodynamics

Physically, charge separation occurs because the Pedersen ion-velocity (\vec{V}_i) is altitude dependent, i.e., ions move faster at higher altitudes than at lower altitudes. (Note that ion motion eventually rotates toward the Hall direction but this occurs at much higher altitudes for metallic ions than molecular ions, typically above 130 km.) This means that for an upward-sloping E_s -layer segment (in altitude versus northward distance transverse to \vec{B}), the \vec{B} field lines become negatively charged because more ions leave than arrive. Conversely, for a downward-sloping segment, the \vec{B} field lines become positively charged. The highly magnetized electrons cannot neutralize this charge accumulation because they cannot move in the Pedersen direction. The charge distribution and corresponding \vec{E}_p that develop are shown schematically in Figure 6. Also, as expected from the requirement for current continuity, \vec{E}_p opposes \vec{E}_0 in regions of high $\Sigma_p^{E_s}$ and augments \vec{E}_0 in regions of low $\Sigma_p^{E_s}$.

To quantify this polarization process, we assume that N is constant and that the variations in $\Sigma_p^{E_s}$ can be estimated from the altitude variations in v_i in the center of the E_s layer. We then require current continuity in the direction of \vec{E}_0 , which gives

$$\bar{E}_p^0 = E_0 \left(\frac{v_i^2 + \Omega_i^2}{v_i} \right) \int \left[\frac{v_i^2 - \Omega_i^2}{(v_i^2 + \Omega_i^2)} \right] \frac{\partial v_i}{\partial y} dy \quad (5)$$

Using (5), we computed E_p^0 / E_0 for two values of altitude modulation, which are plotted in Figure 7. As described above, \bar{E}_p^0 is positive (aligned with \bar{E}_0) when the E_s layer is

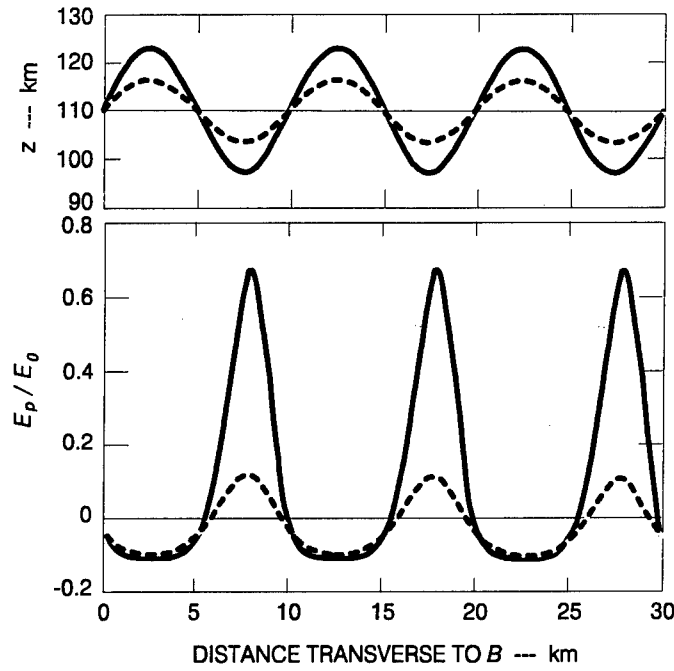


Figure 7 The polarization electric field computed for two amplitudes of altitude modulation.

low in altitude and negative when the E_s layer is high. When the E_s layer is modulated ± 7 km, $E_p^0 \approx \pm 0.1 E_0$ and is essentially negligible, but when the modulation increases to ± 14 km, $E_p^0 \approx \pm 0.7 E_0$. This means that the total electric field would be $1.7 E_0$ where the E_s layer is at low altitudes but small where the E_s layer is at high altitudes. The strength of \bar{E}_p^0 is seen from (5) to depend on the gradient in v_i with respect to the northward transverse distance (y). For a sinusoidally modulated E_s layer with amplitude A and a v_i profile that is exponential in form with a constant scale height H , we have

$$L_v = \left(\frac{1}{v_i} \frac{\partial v_i}{\partial y} \right)^{-1} = \frac{H}{Ak \cos ky} \quad (6)$$

where $k = k_g \sin I$. From (6), \bar{E}_p^0 is proportional to A and can, in principle, be made larger by allowing the AGW to act longer on the E_s layer. In this case, spatial resonance requires that the plasma move in the southwest direction.

The charge and \bar{E}_p^0 distributions are consistent with the observed QP characteristics. Because \bar{E}_p^0 points away from positively charged regions and toward negatively charged regions, the gradient-drift instability would operate along the walls of negatively charged sheets. When \bar{E}_p is added to \bar{E}_0 , the gradient-drift instability is strongest along the equatorward walls of the negatively charged sheets. The fact that the positively charged sheets are stable to the gradient-drift instability is consistent with observations of near-constant range-rates associated with contiguous QP echoes (item 3). The rapid variation in \bar{E}_p with northward distance and the sign reversal is consistent with observations of apparent velocity shear (item 4). *Yamamoto et al.* [1991] presented one set of Doppler velocity measurements (see their Figure 1) in which the mean value varied almost monotonically from +50 m/s at 125-km altitude to about -120 m/s at 108 km. While the variation could be spatial or temporal, they showed that the mean Doppler velocity averaged over perhaps six striations (see their Figure 4) continued to have this same monotonic variation with altitude. Because the radar beam is directed transverse to \bar{B} at all ranges shown, the variation in mean Doppler velocity with altitude corresponds to a variation as a function of transverse distance.

The stability of the geometric shape imposed by the AGW requires some thought because the shear can be substantial. The V_i is zero at 95-km altitude and increases rapidly to about $V_e/2$ at 125-km altitude. For example, if V_e is 50 m/s, V_i would be 25 m/s and would be comparable to the AGW-induced field-aligned ion motion of 35 m/s used above. In this case, the sinusoidal shape would become distorted by a clockwise rotation, as schematically represented by the dash-dotted curve in Figure 6. (Note that the sense of rotation is opposite to that suggested by *Woodman et al.* [1991].) This rotation would lead to a closer alignment of the downward-sloping segment with \bar{B} , further accumulation in positive charge and enhancement of \bar{E}_p^0 . Conversely, the inclination of the upward-sloping segment decreases, with less buildup in excess negative charge and a

correspondingly weaker \bar{E}_p^0 . The redistribution in $\log \Sigma_p^{E_s}$ is represented by the dash-dotted curve in the lower portion of Figure 6. On the other hand, the initial distribution of \bar{E}_p^0 that develops acts to reduce V_i at the higher altitudes and to increase it at the lower altitudes.

Although the actual evolution with time requires further computations, it seems evident that the original shape will not distort as rapidly and will persist longer than might first be expected. This expectation is consistent with the observed stability of striations in QP echoes.

2.3.5 Range-Rate Characteristics

Finally, we consider the relationship of \dot{R} to the tilt and propagation direction of an altitude-modulated E_s layer. A tilt in the sheet that contains the FAI can act to change the azimuthal direction of $\nabla_{\perp} N$ as well as the values of the effective L and the field-line-integrated $\nabla_{\perp} N$. In this sense, a tilted FAI sheet would allow the angular sector of backscatter to be centered on azimuths other than magnetic north.

We construct a simple model in which backscatter is assumed to occur only where the radar line-of-sight intersects a tilted FAI sheet. We begin with the FAI sheet centered in the $x_0 y_0$ plane at $z_0 = 0$. We then perform four coordinate transformations to allow the FAI sheet to be (1) tilted in elevation (α_s) from the horizontal plane, (2) located at an altitude (z_s), (3) rotated in azimuth (β_s), and (4) displaced horizontally (x_s, y_s) from the location of the radar. The following equations express the location of a point on the FAI sheet (x_0, y_0) in terms of the Cartesian coordinates (x, y, z):

$$x - x_s = x_0 \cos \alpha_s \cos \beta_s + y_0 \sin \beta_s \quad (7a)$$

$$y - y_s = -x_0 \cos \alpha_s \sin \beta_s + y_0 \cos \beta_s \quad (7b)$$

$$z - z_0 = x_0 \sin \alpha_s \quad (7c)$$

In these equations, x is eastward, y is northward, and z is upward. The radar is placed at the origin of this coordinate system and has a position vector to a point P in space given by elevation (α), azimuth (β), and range (R) or, in terms of the Cartesian coordinates for point P ,

$$x_p = R \cos \alpha \sin \beta \quad (8a)$$

$$y_p = R \cos \alpha \cos \beta \quad (8b)$$

$$z_p = R \sin \alpha \quad (8c)$$

The case of interest is one in which the point P coincides with a point in the FAI sheet. That solution is obtained by equating x_p , y_p , and z_p from (8) with x , y , and z in (7). This geometry is illustrated in Figure 8.

If we then fix the radar beam in a given direction (α, β) , we can solve for R ,

$$R = \frac{z_s \cos \alpha_s - \sin \alpha_s (x_s \cos \beta_s - y_s \sin \beta_s)}{\sin \alpha \cos \alpha_s + \cos \alpha \sin \alpha_s \sin(\beta_s - \beta)} \quad (9)$$

Differentiating (9) with respect to time, we obtain

$$\dot{R} = \frac{V_z \cos \alpha_s - \sin \alpha_s (V_x \cos \beta_s - V_y \sin \beta_s)}{\sin \alpha \cos \alpha_s + \cos \alpha \sin \alpha_s \sin(\beta_s - \beta)} \quad (10)$$

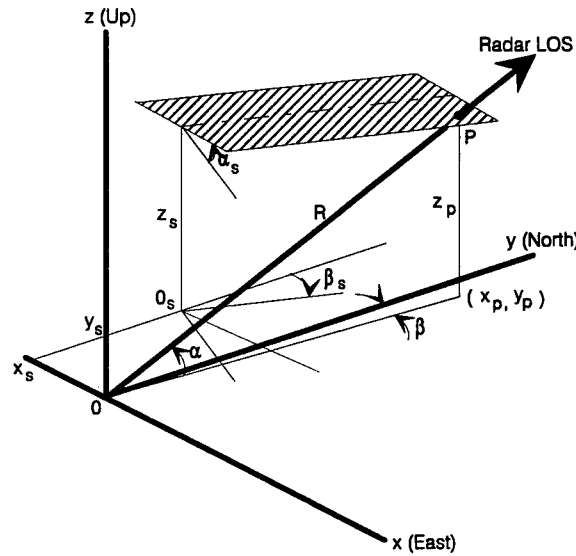


Figure 8 Model of a tilted FAI sheet to explain negative range-rate.

If we assume that the horizontal drift velocity (V_h) is always directed orthogonally (in a clockwise sense) from the major (horizontal) axis of the E_s sheet, we have

$$V_x = V_h \cos \beta_s \quad (11a)$$

$$V_y = -V_h \sin \beta_s \quad (11b)$$

and

$$V_h = V \sin \alpha_v \quad (11c)$$

$$V_z = V \cos \alpha_v \quad (11d)$$

where α_v is the elevation angle of the drift direction. Substituting (11) into (10)

$$\dot{R} = \frac{V \sin(\alpha_v - \alpha_s)}{\sin \alpha \cos \alpha_s + \cos \alpha \sin \alpha_s \sin(\beta_s - \beta)} \quad (12)$$

For an E_s layer altitude-modulated by an AGW, the corresponding orientation of the FAI sheet is one in which $\alpha_s > 0^\circ$ and $V_h > 0$; i.e., the normal to the FAI sheet is directed downward with its horizontal component in the direction of propagation. With this orientation, the FAI sheet has a form that can be related to a plane of constant phase of an AGW.

The general behavior of \dot{R} can be determined from (12). As indicated by the numerator, \dot{R} depends on the relative elevation angle between the velocity vector and the FAI sheet. If the velocity vector is aligned with the FAI sheet, \dot{R} becomes zero. If the sheet is horizontal ($\alpha_s = 0^\circ$), \dot{R} is determined entirely by the vertical velocity, as in the case of a descending E_s layer that might be controlled by tidal winds. On the other hand, if the FAI sheet is vertical ($\alpha_s = 90^\circ$), \dot{R} is controlled entirely by the horizontal velocity and the relative azimuths of the FAI sheet and radar line of sight.

The variation in \dot{R} as a function of the azimuthal direction of sheet propagation is controlled by the denominator in (12). We see from the second term in the denominator that \dot{R} depends on the azimuth of sheet propagation (β_s) relative to the azimuth of the radar beam (β). To illustrate its behavior, we have plotted \dot{R}/V versus $\beta_s - \beta$ in Figure 9, for several fixed values of $\alpha_s > 0^\circ$. We have used 39° as the radar elevation angle and assumed $V_z = 0$. In the case of $\beta = 0^\circ$, $\beta_s = 0^\circ$ corresponds to an FAI sheet that is oriented with its major (horizontal) axis along the north-south direction and is propagating eastward. Correspondingly, $\beta_s = 90^\circ$ refers to equatorward propagation and $\beta_s = 180^\circ$ to westward propagation. At larger angles of β_s , the FAI sheet is propagating with a northward component. The \dot{R} is seen to be always negative regardless of β_s .

Enhanced \dot{R} values are encountered only when the FAI sheet propagates away from the radar.

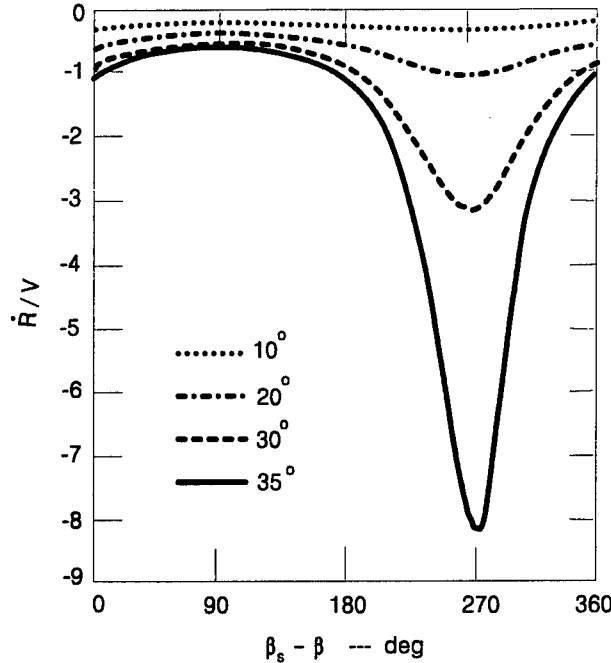


Figure 9 Range rates as a function of FAI sheet propagation direction for different tilt angles.

We have $\dot{R} > 0$ only when the FAI sheet has a component of velocity away from the radar and the tilt angle of the FAI sheet, α_s , is greater than the elevation angle of the radar, α . In the case of the MU radar, the tilt angle would have to exceed 39° . From the AGW dispersion equation and Figure 6, tilts greater than the radar elevation are likely to be common. This result is appealing because we can use it to account for the interferometer observations reported by *Riggin et al.* [1986] in which the drift velocity appeared to be directed toward the northeast. Rather than interpreting the drift to be northeastward, we can interpret those measurements as an example of $\dot{R} > 0$. Given that the radar line of sight was directed toward 65°W true azimuth, an FAI sheet could have been propagating toward the west-southwest and created a geometry in which \dot{R} could be greater than zero. These results suggest that all QP echoes could be produced by AGWs propagating with a southward component in their wave vector and altitude modulation taking place because of ion drag along \vec{B} . This possibility is attractive because altitude modulation is much more difficult to achieve when ion transport must be transverse to \vec{B} .

To summarize, we conclude that \dot{R} is very likely a trace velocity that is associated with backscatter from the intersection of the radar beam with a tilted E_s layer. The ubiquitous presence of $\dot{R} < 0$ in the data and the fact that the mean Doppler velocity behaves independently from \dot{R} attests to this interpretation. In contrast, the mean Doppler velocity is directly related to irregularity motion, and its characteristics should contain information more directly related to the underlying physical process.

2.4 DISCUSSION AND CONCLUSIONS

In this section, we have described an altitude-modulated E_s model and a new polarization process that appears capable of accounting for the QP echoes observed by the MU radar. We have shown that QP echoes are likely produced by radar backscatter from secondary plasma waves generated by the gradient-drift instability. The viewing directions selected for the MU radar have been mostly northward or northeastward; this scattering geometry favors backscatter from secondary waves. Despite poorer radar resolution, there is evidence that the observations of wavelike variations in Doppler velocity reported by *Riggin et al.* [1986] also were QP echoes. Not only are the Doppler velocity variations similar to those of QP echoes, they reported that strong backscatter occurred in two range-gate groups separated by a 22.5-km interval of very weak signals. The echoes at the farther ranges were observed to extend up to 130-km altitude. These characteristics are consistent with the MU radar observations of QP echoes.

We have shown that the secondary plasma waves could be generated, through a cascade process [*Sudan et al.*, 1973], by primary plasma waves whose $\lambda_p < 50$ m. We note that the approximation used by *Sudan et al.* [1973], $\lambda_p \gg \lambda_s$, is reasonably valid for the secondary waves that produce the backscatter detected by the MU radar. At lower radar frequencies, this approximation becomes less valid and is likely accompanied by weaker growth rates. The fact that the wavelengths of the responsible primary waves seem to be short enough not to be seriously affected by polarization-reducing effects suggests that an E_s layer does not have to be altitude modulated to produce QP echoes, as suggested by *Woodman et al.* [1991]. As supporting evidence, we note that *Riggin et al.* [1986] obtained interferometer measurements that indicate radar backscatter can occur from what appears to be an unmodulated E_s layer. There are also a few examples of nighttime MU radar measurements in which echoes are of the continuous type [M. Yamamoto, unpublished data]. These results suggest that QP echoes could be tracers for a process that imposes the large-scale, wavelike features that have been observed. This conclusion

is convenient because if the large-scale wavelike structures are plasma waves generated by the gradient-drift instability, as suggested by *Riggin et al.* [1986], its proper description would have to await a theory that does not exist today. Certainly local theory ($kL \gg 1$) cannot account for λ_p values that are greater than say, $L/4$. Under these conditions, the approximation used by *Kudeki et al.* [1982] to account for long wavelength waves in the equatorial electrojet breaks down. This, of course, is the reason *Riggin and Kadish* [1989] formulated a nonlocal theory for the gradient-drift instability but they used an equatorial geometry which avoids the polarization-reducing issue.

To account for both the large-scale wavelike features and the surprisingly large Doppler velocities, we have shown that an altitude-modulated E_s layer is conducive to the development of \bar{E}_p . We have shown not only that $\Sigma_p^{E_s}$ is comparable to the nighttime Σ_p^F and Σ_p^E , but that the variation in $\Sigma_p^{E_s}$ can range over two orders of magnitude as the E_s layer rises in altitude from 95 to 125 km. The variation in $\Sigma_p^{E_s}$ is produced, in this case, by the near-exponential variation in v_i with altitude rather than in N , which is the usual case. The polarization process, therefore, is shown to arise from a need to maintain a divergence-free Pedersen current in the presence of $\Sigma_p^{E_s}$ variations.

The development of substantial \bar{E}_p^0 values requires strong altitude modulation of the E_s layer, and a form of spatial resonance is needed between the E_s layer and the AGW. For an AGW that propagates with a southward component, spatial resonance is achieved when both plasma and AGW propagate southward together. Both *Riggin et al.* [1986] and *Yamamoto et al.* [1993] have reported observations in which the drift appeared to be toward the southwest, which is consistent with spatial resonance. *Sinno et al.* [1964] also reported E_s signatures in 1.85-MHz LORAN transmissions using a spaced-receiver network and measurements of the time delay of arrival. The data were shown to be consistent with long reflecting strips that were tilted from the horizontal and oriented in the northeast-southwest direction with a preferred propagation direction toward the southwest.

While these results are consistent with the concept of spatial resonance, *Riggin et al.* [1986] also presented a data set in which the drift appeared to be toward the northeast. The northward component of drift would require that the AGW would also have to propagate northward to satisfy spatial resonance. The problem here is that the phase fronts of the AGW could not be aligned with \bar{B} and, without alignment, vertical ion

transport would be very difficult. Instead, we have proposed a different interpretation for their interferometer results. We suggest that the apparent northward motion is simply a trace velocity produced by a tilted FAI sheet that propagated in the west-southwest direction with a component of motion away from the radar. With this interpretation, we can hold to the altitude-modulated E_s model in which the AGW propagates with a southward component.

The actual scenario is, however, likely to be much more complicated. For example, if there is a wind profile in the E region such as that which might have created the E_s layer in the first place, we might expect dynamo electric fields to be generated which would add to the contributions from the F -region dynamo. The strongest dynamo electric fields would come from altitudes where the local conductivity is largest. In this manner, we might also expect further contributions to the total electrostatic field and to the wavelike variations observed in the mean Doppler velocity.

We have, therefore, found that QP echoes from mid-latitude E_s layers arise from a hierarchy of two processes. At the largest scales, AGWs impose kilometer-scale, wavelike altitude-modulations on existing E_s layers, and this structure provides the basic geometry from which primary plasma waves ($\lambda_p < 50$ m) are generated via the gradient-drift instability. The altitude-modulated E_s layer allows generation of an \vec{E}_p which accounts for the large Doppler velocities. The primary plasma waves with enhanced V_{ei} provide the environment for generation of secondary plasma waves detectable by 50-MHz radars. The QP echoes that occur above, say, 130 km altitude are difficult to account for in terms of the gradient-drift instability theory used here. These echoes need to be accounted for either in terms of magnetized ions, a Pedersen current driven instability, or possibly in terms of damped modes that are transported upward by the AGW.

The altitude-modulated E_s model described in this paper predicts that QP echoes are controlled by the following factors:

1. QP echoes are expected to occur when $N \geq 10^5$ el/cm³ under solar minimum conditions; the threshold value for N is likely to be larger under solar maximum conditions.

2. Because strong altitude modulation of an E_s layer is possible only when the AGW propagates southward and has a prolonged interaction with the E_s plasma through spatial resonance, QP echoes are expected to occur only when an E_s layer has a southward component of motion.

3. Because short-scale, primary plasma waves are needed to generate the secondary plasma waves of interest, and because generation of short-scale primary waves require large V_{ei} , \vec{E}_p must develop in order to produce QP echoes. Therefore, large-scale charge separation is also a necessary condition for the occurrence of QP echoes.

3 SPORADIC- E MODELING

3.1 INTRODUCTION

Sporadic E (E_s) remains as one of the foremost obstacles to effective OTHR performance. When present, E_s severely restricts, obscures, and makes ambiguous the area under surveillance. When an E_s layer enters the field of view of an OTHR, it drastically lowers the reflection altitude of the sky-wave signal which, in turn, reduces substantially the one-hop sector that was being viewed. Plasma structure in an E_s layer causes HF signals to be partially reflected and to follow multipaths, both of which lead to target obscuration. True to its label, E_s occurs sporadically and continues to elude useful predictive description except in crude statistical terms. For example, the seasonal occurrence of intense E_s during the day in local summer is well known. Little is known, however, about the shorter-term variability in E_s occurrence. Perhaps even less is known about the plasma structure in E_s layers which makes propagation effects difficult to model. Most of the current propagation models (e.g., AMBCOM [Smith and Hatfield, 1987]) use the Sinno model [Sinno *et al.*, 1976] which has been constructed from the signal statistics of radio measurements made in Japan. How well it extrapolates to other locations and conditions is not known. This clearly undesirable and compromising situation continues to persist even after E_s has been investigated, often intensively, for more than four decades [e.g., see reviews by Whitehead, 1970, 1989].

Progress in the understanding of E_s has slowed since the late 1970s and this trend can be expected to continue for at least three reasons. First, virtually all of the statistical data that exist on E_s were compiled through the scaling of parameters manually from ionograms recorded on film or paper. Improvements to the existing data base are not likely because rescaling of old ionograms would be beyond the scope of resources now available for the E_s problem and this approach would not be cost effective. Many of the ionosonde stations established during the International Geophysical Years (IGY) have been shut down, and ionograms from fewer and fewer ionosonde stations are being scaled routinely. Second, the existing data base does not include signal amplitude, phase, or Doppler information. Without such information, it is extremely difficult to learn more about E_s plasma structure or about propagation effects produced by E_s . Although the number of digital ionosondes that are capable of such measurements is increasing, global coverage with a network as densely distributed as that during the IGY is not likely to be realized in the near future. And third, there are fewer and fewer Department of Defense

(DoD) funds being made available for any comprehensive research of the E_s problem. Experimental programs are clearly needed to obtain a data base on E_s structure and corresponding propagation effects. Without such experimental data, progressive E_s modeling will remain difficult.

Given these circumstances, the only viable approach that will improve our understanding of E_s is to develop a working knowledge of the underlying physical processes that control the production, distribution, and dissipation of E_s . This approach is cost effective because scientific research continues to be funded and steady progress is being made in atmospheric and ionospheric physics. This new and improved knowledge, therefore, can be applied to the E_s problem at little cost to DoD agencies and the OTHR community. For these reasons, we have proceeded to model E_s with this view.

The most puzzling property of E_s in terms of understanding its underlying physics is its statistical occurrence-maximum during the summer. This morphological feature is curiously alluring because it defies interpretation in terms of the well-established wind-shear theory of E_s formation [e.g., *Whitehead*, 1961; *Axford*, 1961]. While wind-shear theory is considered by most to be the only viable mechanism, *Whitehead* [1989] states that it "fails completely to explain the morphology of sporadic E ." In other words, because wind shears are believed to be ever present and not solely a summer phenomenon, the theory by itself cannot account for this summer occurrence maximum. On the other hand, *MacLeod et al.* [1975], after successfully modeling a rather comprehensively measured E_s event with wind-shear theory, concluded that "the sporadic nature of E_s occurrence with time of day and season may be understood as reflecting the meteorological vagaries of the upper atmospheric winds and meteoric influx." Then again, the dominance of E_s morphology by this seasonal maximum could be suggesting that a major player in the systematics of E_s formation has not yet been identified. With substantial progress being made observationally, theoretically, and through modeling efforts in the scientific community regarding our understanding of the coupled dynamical interactions between the ionospheric plasma and the neutral atmosphere, the opportunity has never been better for solving this enigma. With these reasons as the basis, we undertook the task of uncovering the cause of the daytime summer maximum in E_s occurrence.

Our results on E_s modeling are presented in the remainder of this section. Our key finding is the discovery that the morphology of E_s occurrence is controlled primarily

by the variation in direction of the ionospheric electric field (\vec{E}) as a function of local time and season. We show, for the first time, that the seasonal E_s occurrence is controlled by the corresponding availability of metallic ions in the upper E region. We begin in Section 3.2 with a brief review of E_s morphology and the status of knowledge regarding the distribution of metallic ions in the ionosphere. We then derive, in Section 3.3, the ion transport equations that include the wind-shear theory of E_s . We use these equations, in Section 3.4, to show how the ionospheric electric field controls the availability of metallic ions in the upper E and lower F regions and how the seasonal behavior of this reservoir of metallic ions is consistent with the seasonal occurrence pattern for E_s . We close with a discussion of these findings in Section 3.5.

3.2 REVIEW OF E_s

3.2.1 Morphological Features of Interest

The E_s features of interest in our pursuit of the underlying physical processes include the diurnal, seasonal, and solar cycle dependences of E_s occurrence. Much effort has already been expended by previous researchers to obtain statistical descriptions of E_s [e.g., *Smith*, 1957; *Kasuya*, 1958; *Basu et al.*, 1973]. We have selected the E_s morphology over Kokubunji, Japan (35.7°N, 139.5°E) for analysis because its geographic location is similar to that of the MU radar (34.9°N, 136.1°E) whose \vec{E} measurements will be used to demonstrate \vec{E} control of E_s occurrence (Section 3.4). The diurnal-seasonal occurrence pattern of E_s for this location is presented in Figure 10, reproduced from *Smith* [1968]. The occurrence (in time) of intense E_s ($f_oE_s \geq 10$ MHz) is shown by contours of constant percentage values as a function of local time (LT) and month of the year. (The data, obtained between 1958 and 1966, span years of both high and low solar activity.)

The first two features of interest, the diurnal and seasonal variations in E_s occurrence, are seen to have distinctive patterns in Figure 10. Diurnally, E_s occurrence rapidly increases shortly after sunrise, peaks during the prenoon hours, and gradually decays during the night. The decay, however, is not monotonic from the prenoon hours, as indicated by the presence of a local minimum around sunset. To evaluate the importance of this secondary feature, we examined the E_s occurrence curves for $f_oE_s \geq 10$ MHz obtained at three ionosonde stations, including Kokubunji, which are

reproduced from *Smith* [1968] in Figure 11. While appearing relatively unimportant

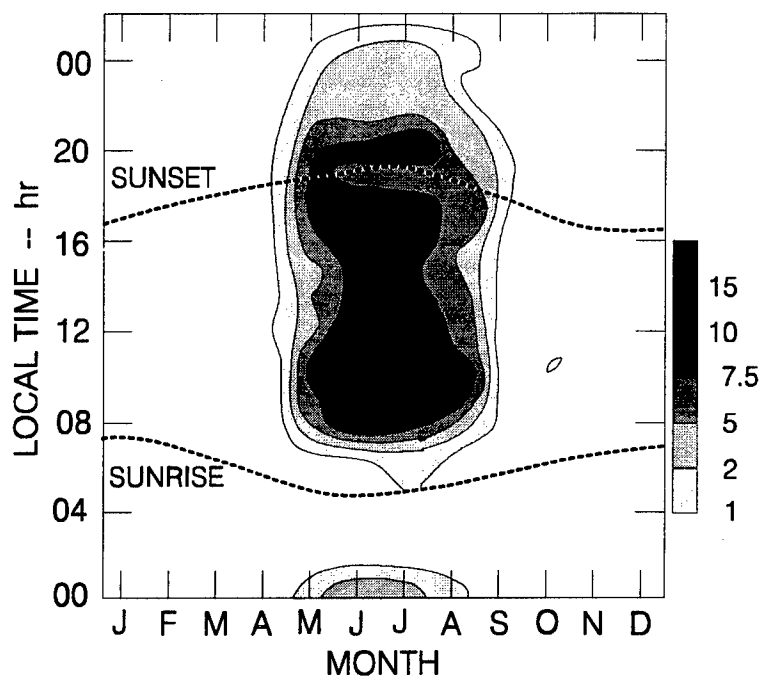


Figure 10 Occurrence frequency percentage of intense E_s for $f_o E_s \geq 10$ MHz at Kokubunji, Japan (1958-1966); reproduced from *Smith* [1968].

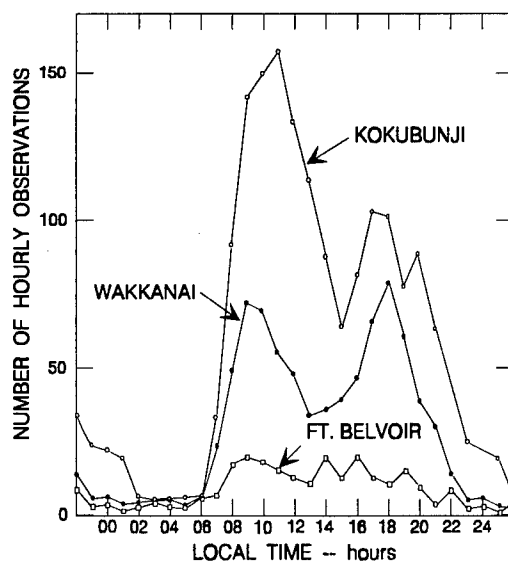


Figure 11 Diurnal variation in the occurrence of intense E_s ($f_o E_s \geq 10$ MHz) at three ionosonde stations: Kokubunji and Wakkanai, both in Japan, and Ft. Belvoir, Virginia (reproduced from *Smith*, 1968)].

compared to the primary maximum in Figure 10, this secondary maximum can be seen in Figure 11 to be a distinct morphological feature. The Kokubunji curve (1957 to 1966 data) clearly displays a primary maximum around 1000 LT and a secondary maximum around 1800 LT. The same double humped shape is more apparent in the Wakkanai curve (1958 to 1966 data) where the two maxima have nearly identical values (in the number of hourly occurrences); the two peaks appear around 0900 and 1800 LT with a minimum between the two at 1300 LT. On the other hand, there is little evidence of the two-humped shape in the Ft. Belvoir curve (1957 to 1966 data). The features of interest in the diurnal variation of E_s occurrence are the rapid increase shortly after sunrise, the primary maximum around mid-morning, and the secondary maximum around local sunset or early evening.

The second morphological feature of interest, the seasonal distribution in E_s occurrence, is seen in Figure 10 to consist of a strong maximum in the summer (with the percentage occurrence exceeding 15 percent in June and July) and abrupt decreases in percentage occurrence in May and September leading to a virtual absence of intense E_s during the equinoxes and winter. Others have reported similar findings but in some cases with a less prominent secondary maximum in local winter [e.g., *Smith*, 1957, 1968; *Basu et al.*, 1973]. This occurrence of a prominent maximum during local summer has defied interpretation until now (Section 3.4).

The third morphological feature of interest, the solar activity dependence of E_s occurrence, is illustrated in Figure 12 where we present the percentage occurrence of E_s for $fE_s > 5$ MHz and for $fE_s > 7$ MHz, again for Kokubunji, over eight consecutive years. These curves, reproduced from *Kasuya* [1958], illustrate convincingly the virtual independence of E_s occurrence from solar activity. We see that the maxima in E_s occurrence all occur during the summer (which illustrates the persistence of the seasonal behavior) and the values of the maxima are all about 60 percent for $fE_s > 5$ MHz and about 30 percent for $fE_s > 7$ MHz, regardless of year. This independence from solar activity variations is another morphological property that should be accounted for by any viable theory of E_s formation. (Curiously, there appears to be a weak four-year modulation in occurrence percentage in the $fE_s > 5$ MHz. This modulation, however, is not seen in the $fE_s > 7$ MHz occurrence pattern.)

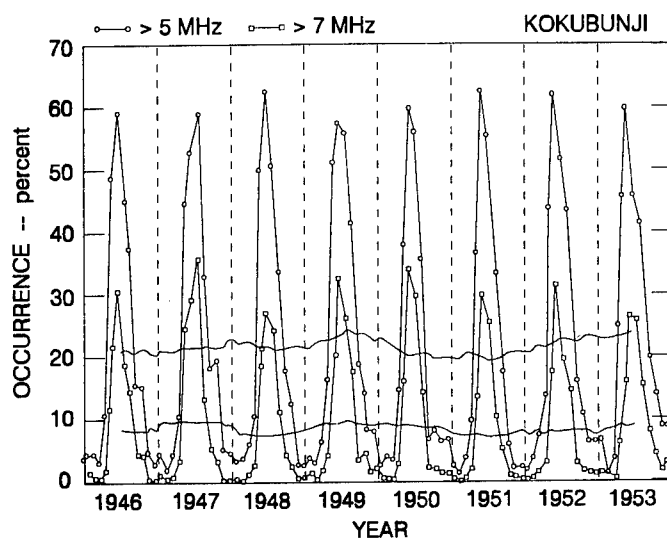


Figure 12 Long-term occurrence of E_s at Kokubunji, Japan over eight consecutive years (reproduced from *Kasuya* [1958]).

3.2.2 Existing Theories for Summer Maximum in E_s Occurrence

Several theories have been proposed to account for the seasonal behavior of mid-latitude E_s . *Triskova* [1974] suggested that the altitude of mean wind shear is higher in summer where ion convergence is stronger. *MacDougall* [1978] suggested that the semidiurnal zonal winds have maximum amplitudes in local summer. *Koren'kov* [1979] and *Koren'kov and Deminov* [1980] suggested that the seasonal behavior of neutral-wind direction is the source of the summer maximum in E_s occurrence. As evidence, *Koren'kov* [1979] referred to *Vergasova et al.* [1977] in which the preferred direction of the mean \bar{U} (between 100 and 200 km altitude) is toward the northeast (NE) in summer and toward the southwest (SW) in winter under solar minimum conditions. *Nygren et al.* [1984] performed a more detailed analysis of this mechanism and concluded that this mechanism must be considered as a potential source of E_s at high latitudes but that it is not likely to be effective at lower latitudes where \bar{E} must be very small. As evidence against the viability of this mechanism at temperate latitudes, they referred to the two maxima in the diurnal occurrence pattern of E_s [e.g., *Smith*, 1968] and the temporal behavior of the altitude of E_s layers [*MacDougall*, 1974, 1978] and concluded that these features are more consistent with the wind-shear mechanism driven by the semidiurnal component of the atmospheric tide. (They do not, however, show how wind-shear theory can produce a summer maximum in occurrence frequency.)

While the concepts put forth to account for the seasonal behavior of E_s occurrence are perhaps reasonable, the experimental measurements used to infer \vec{U} profiles and tidal modes remain questionable. Another difficulty is that the assumption of a steady supply of metallic ions remains to be validated. Once metallic ions are swept toward a wind shear node and transported downward by the tidal wind system, how are the metallic ions replenished?

3.2.3 Metallic Ions

Our knowledge of metallic-ion circulation and distribution in the ionosphere is still rudimentary. (The difficulty is that trace ion constituents can only be detected in the ionosphere in situ with ion mass spectrometers.) It is clear that metallic ions are of meteoric origin because their relative concentrations have been found to be very similar to their composition in meteors [Swider, 1984]. The peak altitude for deposition of metallic atoms through meteor ablation is near 92 km [e.g., Narcisi, 1968; Swider, 1984]. In their neutral form, metallic atoms are not likely to migrate in altitude because winds are, for the most part, directly horizontally. Metallic ions, however, are easily produced through ionization by solar radiation and through charge exchange with O_2^+ and NO^+ ; once ionized, their lifetimes can be weeks [e.g., Mende *et al.*, 1985]. In this ionized form, they are susceptible to transport by \vec{E} and \vec{U} (through ion drag). An apparently serious difficulty is that these forces are reduced considerably at altitudes below 95 km because of ion-neutral collisions. Metallic ions, therefore, were not envisioned to participate in any ionospheric circulation pattern.

In situ observations of significant amounts of metallic ions in the upper ionosphere have confirmed that they do circulate and have forced us to seek mechanisms that can transport these ions upward in altitude from below 100 km into the upper ionosphere. Hanson and Sanatani [1970], for example, reported the presence of Fe^+ ions above the F_2 peak from data collected with a retarding potential analyzer aboard the Ogo-6 satellite. They suggested that these ions simply rise during the day at equatorial latitudes through $\vec{E} \times \vec{B}$ plasma-drift motion.. Hanson *et al.* [1972] performed a more quantitative analysis and showed that upward ion transport is confined to the equatorial electrojet region, within a few degrees of the dip equator. They assumed a Chapman profile for the metallic ions with a peak at 93 km altitude, and showed that the vertical Pedersen ion drift in the electrojet (greatly enhanced there by the vertical polarization \vec{E})

is capable of extracting ions out of the source region and transporting them up into the F layer. At higher latitudes, the vertical \vec{E} is smaller and the upward drift would be partially offset by downward diffusion. Without knowledge of the nighttime electrodynamics, they did not attempt to model the return flow of ions from the F layer back to the lower ionosphere.

Kumar and Hanson [1980] found, for the first time, from AE-C satellite data that metallic ions exist in the F -region ionosphere at all latitudes and longitudes, in sharp contrast to findings from the Ogo-6 data. They noted that the equatorial Pedersen ion fountain, proposed by *Hanson et al.* [1972], could not account for the ion distribution observed in AE-C data; however, the observed distribution must be produced somehow by ion transport. They suggested a role for the thermospheric neutral wind. As an example, they noted that metallic-ion profiles obtained by rockets were consistent with a mid-latitude thermospheric wind directed poleward during the day and equatorward during the night, which is consistent with a wind blowing away from the subsolar point. They also noted that the high correlation in the occurrence of other metallic species with widely varying masses suggest that gravity and field-aligned motion (both of which are mass dependent) are not dominant forces in the circulation of metallic ions.

Grebowsky and Pharo [1985] showed, also from AE-C data, that metallic ions in the F layer are most prevalent in the equatorial and polar regions with a distinct minimum at middle latitudes. While the equatorial population appeared to be consistent with a vertical ion transport mechanism proposed by *Hanson et al.* [1972], they concluded that the equatorial mechanism must be distinct from a polar mechanism. For the polar mechanism, they suggested Pedersen ion drift produced by large electric fields associated with subauroral ionospheric drift events. There have not been any investigations into the circulation pattern associated with metallic ions in mid-latitude regions.

While little is yet known about the circulation and distribution of metallic ions at mid-latitudes, we now know that they are found at ionospheric altitudes in significant amounts. Allowance for their presence in the ionosphere through circulation eliminates the need to rely on direct meteoric deposition for a supply of metallic ions. This conclusion is consistent with the lack of direct correlation found between meteor activity and E_s occurrence [e.g., *Hedberg*, 1976, *Ellyett and Goldsbrough*, 1976]. If metallic-ion distribution is determined by transport, the controlling force is likely to be at least one of the following: \vec{E} , \vec{U} , or wind shear. While these forces have been considered as a source

of ion convergence, they have not been examined in terms of ion circulation. Of the three, \vec{E} is most likely to be playing the dominant role. It results from charge separation produced in dynamo regions where gradients in conductivity or divergences in \vec{U} are nonzero. Typically, the dynamo regions are in the E layer during the day and in the F layer during the night. The \vec{E} that results from these two regions will transport the ions through $\vec{E} \times \vec{B}$ motion at high altitudes and through Pedersen drift at low altitudes. In contrast, the only \vec{U} of importance is that in the E region where it imposes influence on ions through ion-neutral collisions. While \vec{U} can modify the metallic-ion distribution in the E region, it is not a factor when metallic ions leave the E region. Similarly, wind shears can modify the ion distribution but on even more local scales.

3.3 ION TRANSPORT EQUATIONS

In this section, we derive the ion transport equations that are used in Section 3.4 to analyze both the circulation pattern of metallic ions in the ionosphere and their convergence properties. As discussed in that section, we are most interested in where metallic ions go in altitude when placed under the influence of a diurnally varying \vec{E} and \vec{U} . We, therefore, derive expressions for the vertical component of the ion velocity. For completeness and their possible use in future analysis, however, we also include the corresponding expressions for the horizontal components. The same ion-transport equations can be used to evaluate the convergence properties, those that determine the rate at which an E_s layer can form. *Chimonas and Axford* [1968] and *MacLeod et al.* [1975], among others, have shown that electron dynamics are inconsequential in this kind of description and can be ignored.

The forms of the resultant equations are not particularly new; they have been presented by others in various subsets or in related forms. The same equations have been used to describe various aspects of wind-shear theory for E_s formation [*Whitehead*, 1961; *MacLeod*, 1966]. *Chimonas and Axford* [1968] showed that the E_s layer moves downward with the phase velocity of the tidal wind. The formation of an E_s layer by a uniform \vec{U} was presented by *Rowe and Gieraltowski* [1974]. The importance of the direction of \vec{E} and altitude-independent \vec{U} in E_s formation was shown by *Koren'kov* [1979], *Koren'kov and Deminov* [1980], and *Nygren et al.* [1984].

3.3.1 Basic Equations

Because E_s forms with a time scale of about 1000 s [e.g., *MacLeod et al.*, 1975] that is long compared to the lifetimes of molecular ions, metallic atomic ions which have much longer lifetimes [e.g., *Rees et al.*, 1976] are believed to play a major role and, indeed, metallic ions have been detected in E_s layers [e.g., *Behnke and Vickrey*, 1975]. For our purposes here, we assume that only metallic ions are present and simply consider the transport of ions by \vec{U} and \vec{E} . We use a Cartesian coordinate system in which the x axis is directed toward geomagnetic east, the y axis toward geomagnetic north, and the z axis is vertically upward. The geomagnetic field, \vec{B} , is in the yz -plane and makes an angle I with the horizontal (i.e., $\tan I = -B_z / B_y$).

The basic equations governing this behavior are the momentum conservation equations, one for each charged species. Assuming quasi-equilibrium conditions, we have

$$q_\alpha (\vec{E} + \vec{V}_\alpha \times \vec{B}) - m_\alpha \nu_\alpha (\vec{V}_\alpha - \vec{U}) = 0 \quad (13)$$

where α refers to either ions (i) or electrons (e), q_α is the charge, \vec{E} is the total electrostatic field, \vec{V}_α is the velocity, and ν_α is the collision frequency of the charged particle species with the neutrals. We can separate (13) into components parallel and transverse to \vec{B} . Taking the parallel component of the momentum equation, we solve for the parallel electric field, $E_{||}$, given by

$$E_{||} = \frac{\nu_\alpha B}{\Omega_\alpha} (V_{||\alpha} - U_{||}) \quad (14)$$

where in (14) the sign of the charged particle is contained in Ω_α . For the cases of interest, the parallel electric field is zero and (14) requires that both the electrons and ions move with the parallel component of \vec{U} . Next, we can solve (13) for the transverse velocity of the charged particles

$$\vec{V}_{\perp\alpha} = \left(\frac{\Omega_\alpha^2}{\Omega_\alpha^2 + \nu_\alpha^2} \right) \frac{\vec{E}_\perp \times \vec{B}}{B^2} + \left(\frac{\nu_\alpha \Omega_\alpha}{\Omega_\alpha^2 + \nu_\alpha^2} \right) \frac{\vec{E}_\perp + \vec{U}_\perp \times \vec{B}}{B} + \left(\frac{\nu_\alpha^2}{\Omega_\alpha^2 + \nu_\alpha^2} \right) \vec{U}_\perp \quad (15)$$

If we define $\rho_\alpha \equiv v_\alpha / \Omega_\alpha$, we can rewrite (15) as

$$\vec{V}_{\perp\alpha} = \left[B(1 + \rho_\alpha^2) \right]^{-1} \left[\vec{E}_\perp \times \hat{b} + \rho_\alpha (\vec{E}_\perp + \vec{U}_\perp \times \vec{B}) + \rho_\alpha^2 \vec{U}_\perp B \right] \quad (16)$$

where \hat{b} is a unit vector in the direction of \vec{B} . (The sign of the charge is preserved in Ω_α and ρ_α .) The sign of the charged species is seen to affect only the second term in (16), that is, the Pedersen drift direction. For electrons, $\rho_e \ll 1$, and (16) becomes

$$\vec{V}_{\perp e} \approx \frac{\vec{E}_\perp \times \hat{b}}{B} \quad (17)$$

In the following, we derive the vertical and horizontal ion velocities that are produced by a neutral-wind shear in altitude, and by altitude-independent components of \vec{E} and \vec{U} .

3.3.2 Ion Velocity from Neutral Wind

We assume a neutral-wind system which consists of two components, one that is altitude independent and another that is associated with the diurnal (or semidiurnal) solar tidal force. The prevailing component, \vec{U}_0 , is directed horizontally along a magnetic azimuth, β_U , and the tidal component has a horizontal wind vector of constant amplitude, U_t , which rotates clockwise (CW) with increasing altitude when viewed from above (left-hand circular polarization). This wind system is described by the following expressions for the eastward (x) and northward (y) components

$$U_x(z, t) = U_{0x} - U_t S_t \quad (18a)$$

$$U_y(z, t) = U_{0y} - U_t C_t \quad (18b)$$

where $U_{0x} = U_0 \sin \beta_U$, $U_{0y} = U_0 \cos \beta_U$,

$$S_t \equiv \sin[k_t(z - z_0) + \omega_t t] \quad (19a)$$

$$C_t \equiv \cos[k_t(z - z_0) + \omega_t t] \quad (19b)$$

and $k_t = 2\pi / \lambda_t$ is the wave number and λ_t is the wavelength. The tidal wind propagates downward ($-z$ direction) with a phase velocity, ω_t / k_t . The periods ($2\pi / \omega_t$) of the

semidiurnal and diurnal tides are 12 and 24 hours. The described tidal wind pattern with an E_s layer situated at the node for EW wind shear is shown sketched in Figure 13.

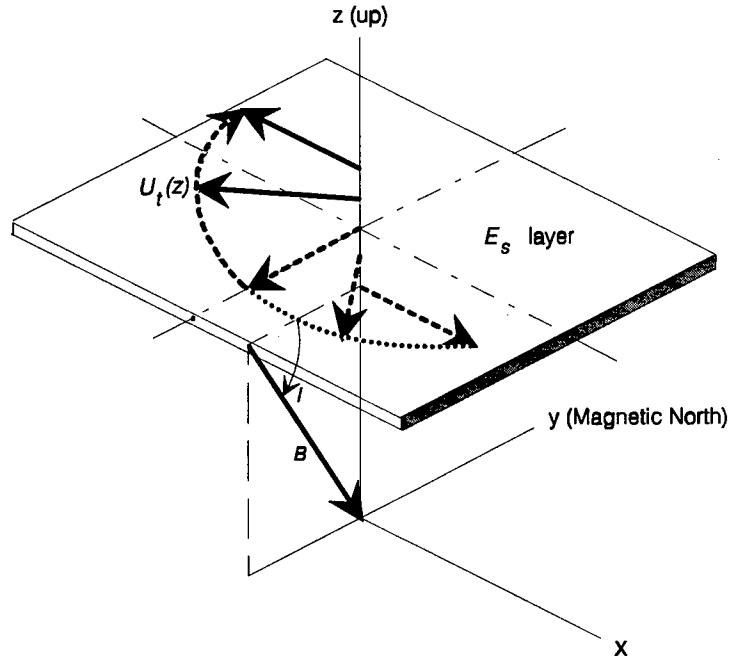


Figure 13 Schematic drawing of an E_s layer situated at an east-west node of a left-circularly polarized, tidal wind profile.

To have ion convergence close to $z = z_0$ from a CW rotation and a shear in the east-west (EW) wind component, we have chosen $U_{tx}(z,0) > 0$ (< 0) where $z < z_0$ ($> z_0$) and $U_{ty}(z_0,0) = -U_t$; at $z = z_0$ when $t=0$. To place a north-south (NS) shear at $z = z_0$, a 90° phase shift should be added to (19a) and (19b). This tidal wind model is generally consistent with most observations. *Hines* [1966] modeled wind measurements made from rocket-released vapor trails and found a diurnal component which could be characterized by a CW rotation with an elliptic polarization, a vertical wavelength of 20 km, and a maximum amplitude of about 50 m/s at 105-km altitude.

Because we are interested in ion motion produced by this wind system in the E and lower F regions, we rewrite (18) in terms of wind components transverse to \vec{B} (U_\perp),

$$U_{\perp x}(x, y, z, t) = U_x(z, t) \quad (20a)$$

$$U_{\perp yz}(x, y, z, t) = U_y(z, t)S_I \quad (20b)$$

and the wind component parallel to \vec{B} , which is given by

$$U_{||}(x, y, z, t) = U_y(z, t) C_I \quad (20c)$$

where $S_I \equiv \sin I$, $C_I \equiv \cos I$, and I is the magnetic inclination (dip) angle. Note that $U_{||} > 0$ in the direction of \vec{B} (i.e., with a downward component in the northern hemisphere) and $U_{\perp yz} > 0$ in the $+yz$ -plane.

The components of ion motion produced by the wind component parallel to \vec{B} can be obtained from (20c). As discussed above, (14) states that

$$V_{||} = U_{||} \quad (21)$$

for situations of interest. From (20c) and (21), we have

$$V_{||} = U_y C_I \quad (22)$$

The horizontal (y) and vertical (z) components of (22) are given by

$$V_{||y} = U_y C_I^2 \quad (23a)$$

$$V_{||z} = -U_y C_I S_I \quad (23b)$$

The sign of (23b) is selected so that $V_{||z} > 0$ when directed along the positive z axis. Note that (23b) must be combined with the contribution from the transverse ion motion in order to obtain the total vertical drift (see below). For example, at low altitudes, the ions are unmagnetized and move only horizontally with the neutral wind which itself is horizontal. But if (23b) is used by itself, the vertical ion motion would be nonzero.

The components of ion motion produced by the wind contributions transverse to \vec{B} , given by (20a) and (20b), are obtained as follows. Neglecting \vec{E} , (17) for ions becomes

$$\vec{V}_{\perp} = \frac{\rho}{1 + \rho^2} \left[(\vec{U}_{\perp} \times \hat{b}) + \rho \vec{U}_{\perp} \right] \quad (24)$$

where we have dropped the subscript for ions. Substituting (20a) and (20b) into (24), the horizontal eastward component of ion motion is given by

$$V_{\perp x} = \frac{\rho}{1+\rho^2} [\rho U_x - U_y S_I] \quad (25)$$

Because there are no contributions from parallel wind motion to the x component of ion motion, (25) is the total horizontal ion drift in the eastward direction produced by the neutral wind. The ion motion transverse to \vec{B} and in the northward vertical plane is given by

$$[V_{\perp}]_{yz} = \frac{\rho}{1+\rho^2} [U_x + \rho U_y S_I] \quad (26)$$

The horizontal, northward (y) component of (26) is then given by

$$V_{\perp y} = \frac{\rho S_I}{1+\rho^2} [U_x + \rho U_y S_I] \quad (27)$$

and the vertical (z) component of (26) is given by

$$V_{\perp z} = \frac{\rho C_I}{1+\rho^2} [U_x + \rho U_y S_I] \quad (28)$$

The total ion velocity in the vertical direction produced by the neutral wind is obtained by combining (23b) and (28),

$$[V_z]_U = \frac{C_I}{1+\rho^2} [\rho U_x - U_y S_I] \quad (29)$$

Equation (29) provides the basis for ion convergence as the means of E_s formation, which is considered in Section 3.3.4. The altitude dependence of vertical ion motion on the wind components can be seen in (29). At low altitudes ($\rho \gg 1$), the vertical ion velocity is determined by the transverse ion motion produced by the east-west (EW) component (first term in (29)). At high altitudes ($\rho \ll 1$), the vertical ion velocity is determined by ion drag by the north-south (NS) component of \vec{U} [second term in (29)].

Setting $U_t = 0$, we have the expression for the altitude-independent neutral wind,

$$[V_z]_{U_0} = \frac{U_0}{1 + \rho^2} [\rho \sin \beta_U - \cos \beta_U S_I] C_I \quad (30)$$

which is identical to Eq.(12) in *Nygren et al.* [1984]. Finally, the total horizontal, northward component of ion velocity is obtained by combining (23a) and (27)

$$[V_y]_U = (1 + \rho^2)^{-1} [\rho S_I U_x + (\rho^2 + C_I^2) U_y] \quad (31)$$

3.3.3 Ion Velocity from Electric Field

Neglecting the wind terms in (16), we have

$$\vec{V}_\perp = [B(1 + \rho^2)]^{-1} [\vec{E}_\perp \times \hat{b} + \rho \vec{E}_\perp] \quad (32)$$

where \vec{E}_\perp is assumed to be directed along a magnetic azimuth β_E such that $E_x = E_\perp \sin \beta_E$ and $E_y = E_\perp \cos \beta_E$. The two orthogonal components of (32) are

$$[V_{\perp x}]_E = [B(1 + \rho^2)]^{-1} (\rho E_x - E_{yz}) \quad (33a)$$

and

$$[V_{\perp yz}]_E = [B(1 + \rho^2)]^{-1} (E_x + \rho E_{yz}) \quad (33b)$$

Then the horizontal components are

$$[V_x]_E = [B(1 + \rho^2)]^{-1} (\rho E_x - E_{yz}) \quad (34a)$$

$$[V_y]_E = [B(1 + \rho^2)]^{-1} (E_x + \rho E_{yz}) S_I \quad (34b)$$

and the vertical component is

$$[V_z]_E = [B(1 + \rho^2)]^{-1} (E_x + \rho E_{yz}) C_I \quad (34c)$$

which is identical to Eq.(8) in *Nygren et al.* [1984]. We can also write (34c) as

$$[V_z]_E = \frac{E/B}{1+\rho^2} [\sin \beta_E + \rho \cos \beta_E] C_I \quad (35)$$

All of the ion circulation computations in Section 3.4 have been made using (35).

3.3.4 Ion Convergence

Expressions for ion convergence produced by \vec{E} and \vec{U} are obtained from the ion continuity equation,

$$\frac{\partial N}{\partial t} = P_i - L_i - \nabla \cdot (N \vec{V}) \quad (36)$$

where N is the ion number density, P_i is the ion production rate, and L_i is the radiative recombination loss rate. For our purposes here, we ignore production, loss, and gradients in the horizontal direction. We then have

$$\frac{\partial N}{\partial t} = -N \frac{\partial V_z}{\partial z} - V_z \frac{\partial N}{\partial z} \quad (37)$$

The second term in (37) is negligible during the early stages of E_s formation but does play a role in the final configuration of the E_s layer. We neglect the second term because we are most interested in the role of \vec{E} in ion convergence in a general sense and not in detail. Ion convergence is defined by

$$Q \equiv -\frac{\partial V_z}{\partial z} \quad (38)$$

Substituting (38) into (37) and solving for N ,

$$N(z,t) = N(z,0) \exp \int Q(z,t) dt \quad (39)$$

Rather than solving (39), we restrict our analysis to an evaluation of Q . Differentiating (29) and then substituting into (38), we have the ion convergence produced by \vec{U} ,

$$Q_U = -\frac{\partial[V_z]_U}{\partial z} = -\frac{C_I}{1+\rho^2} \left[\left[\frac{(1-\rho^2)U_x + 2\rho U_y S_I}{1+\rho^2} \right] \frac{\partial \rho}{\partial z} + \rho \frac{\partial U_x}{\partial z} - S_I \frac{\partial U_y}{\partial z} \right] \quad (40)$$

From (40) we see that if \vec{U} has an altitude profile without the altitude independent term, the wind-shear (i.e., last two) terms come into play. And, as expected from well-known wind-shear theory, the EW wind profile controls Q_U at low altitudes while the NS wind profile controls Q_U at high altitudes.

Similarly, differentiating (35) and substituting into (38), we have the ion convergence produced by \vec{E} ,

$$Q_E = -\frac{\partial[V_z]_E}{\partial z} = \frac{E/B}{1+\rho^2} \frac{\partial \rho}{\partial z} \left[\frac{2\rho}{1+\rho^2} \sin \beta_E - \frac{(1-\rho^2)}{1+\rho^2} \cos \beta_E \right] C_I \quad (41)$$

And, from (40) and (41), Q_U and Q_E are controlled by the ρ profile if the wind is altitude independent.

Evaluating (41) at $[V_z]_E = 0$,

$$[Q_E]_{z_0} = -\left[\frac{\partial[V_z]_E}{\partial z} \right]_{z_0} = \frac{E}{B} \left(\frac{\partial \rho}{\partial z} \right)_{z_0} \cos^3 \beta_E C_I \quad (42)$$

This result is identical to Eq.(11) in *Nygren et al.* [1984]. The ion dynamics that leads to ion convergence by a uniform \vec{E} is schematically illustrated in Figure 14. The case of interest occurs when \vec{E} is in the NW quadrant or, equivalently, when the electron drift velocity (\vec{V}_e) is in the SW quadrant. The counter-clockwise rotation of the ion velocity with altitude is represented by the set of arrows emanating from the origin (and labeled V). When the ion velocity is in the NW quadrant, its vertical component is directed upward, indicated by the arrows drawn perpendicular to the abscissas. When the ion velocity rotates into the SW quadrant, the sign of its vertical component reverses. Ions, therefore, converge toward the altitude where the ion velocity is westward.

Similarly, ion convergence for an altitude-independent \vec{U} is given by

$$Q_U = -\frac{\partial[V_z]_U}{\partial z} = -\frac{U_0}{(1+\rho^2)^2} \frac{\partial \rho}{\partial z} \left[(1-\rho^2) \sin \beta_U + 2\rho \cos \beta_U S_I \right] C_I \quad (43)$$

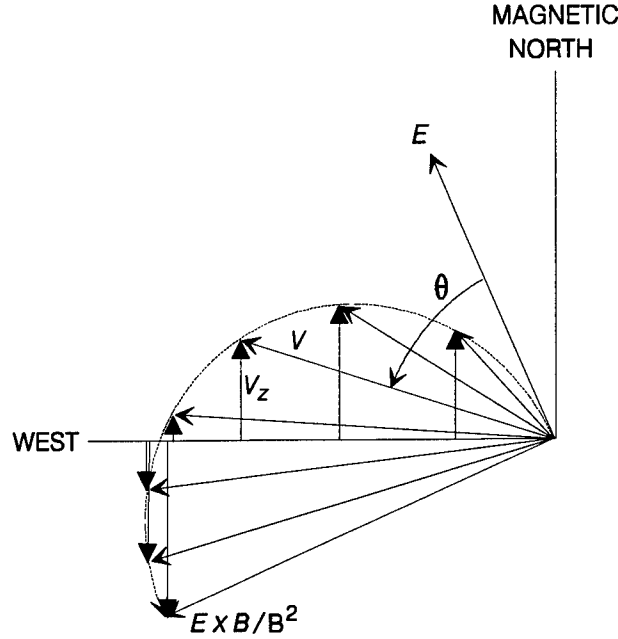


Figure 14 Vector orientation of the ionospheric electric field that produces convergent ion motion in the E region.

Evaluating (43) at $[V_z]_U = 0$,

$$[Q_U]_{z_0} = -\frac{U_0 \tan^2 \beta_U}{(\tan^2 \beta_U + S_I^2)^2} \left(\frac{\partial \rho}{\partial z} \right)_{z_0} \left[\sin \beta_U (\tan^2 \beta_U - S_I^2) + 2S_I^2 \right] C_I \quad (44)$$

From (29), $[V_z]_U = 0$ at $t = 0$ occurs at an altitude where

$$U_t \left(S_t - \frac{S_I}{\rho} C_t \right) = U_{0x} - \frac{S_I}{\rho} U_{0y} \quad (45)$$

Setting $U_t = 0$ in (45), we solve for ρ

$$\rho = S_I \frac{U_{0y}}{U_{0x}} = \frac{S_I}{\tan \beta_U} \quad (46)$$

which is the same as Eq.(13) in *Nygren et al.* [1984]. For the altitudes of interest, $\rho \geq 1$ and $S_I < 1$. This means that the vertical ion velocity becomes zero at these altitudes only when $0 < \beta_U < 90^\circ$; i.e., when \vec{U}_0 is directed toward the NE. In other words, as expected, $\vec{U}_0 \times \vec{B}$ can be added to \vec{E} to compute the effective electric field and ion convergence would occur when that electric field, is directed in the NW quadrant. This result was first reported by *Koren'kov* [1979] and later elaborated on by *Koren'kov and Deminov* [1980] and *Nygren et al.* [1984].

3.3.5 Horizontal Ion Motion

The horizontal ion velocity is given by

$$|V_h|_U = \sqrt{V_{\perp x}^2 + (V_{\parallel y} + V_{\perp y})^2} \quad (47)$$

where the terms in (47) are given by (23), (26) and (28). The magnetic azimuth is given by

$$\tan[Az]_U = \frac{V_{\perp x}}{V_{\parallel y} + V_{\perp y}} \quad (48)$$

or

$$\tan[Az]_U = \frac{\rho U_x - U_y S_I}{U_x S_I + \rho U_y + \rho^{-1}} \quad (49)$$

When $U_t = 0$, (49) becomes

$$\tan[Az]_U = \frac{\rho U_{0x} - U_{0y} S_I}{U_{0x} S_I + \rho U_{0y} + \rho^{-1}} \quad (50)$$

(We expect that the azimuth of the horizontal ion velocity will be westward.) The other case is when there is a tidal component but no prevailing component. At low altitudes

($\rho \gg 1$), $V_x \approx U_x$ and $V_y \approx U_y$. This means that when z_0 is low, the ions there must be moving southward at the neutral wind speed. At higher altitudes, the altitude of zero vertical ion velocity is higher than z_0 ; and if the ions are still following the neutrals, the ion velocity vector must then be directed slightly west of south. The ion motion is completely horizontal at this altitude.

3.4 ELECTRIC FIELD CONTROL

In this section, we show that the distinct diurnal-seasonal behavior of E_s occurrence seen in Figure 10 is controlled largely by the availability of metallic ions. We show that the local metallic-ion supply depends on the diurnal circulation pattern of those ions in altitude and that this pattern is controlled by the ionospheric \vec{E} . We show that there is a funneling effect that increases the local concentration of ions when \vec{E} is directed in the NW quadrant. When this concentration of metallic ions descends into the upper E region where wind shears are effective, E_s forms through further ion convergence via the ever-present tidal wind shears [Harper *et al.*, 1975]. This investigation into the role of \vec{E} was made possible by the recent availability of \vec{E} measurements from the MU incoherent-scatter radar in Shigaraki, Japan [Oliver *et al.*, 1993].

In the following, we present the ion circulation patterns produced by the \vec{E} results in Oliver *et al.* [1993], using the vertical ion transport equations derived in the previous section. We first present the seasonal behavior of this diurnal circulation pattern and then illustrate the lack of solar activity dependence.

3.4.1 Average Ion Circulation Patterns

The \vec{E} values from Oliver *et al.* [1993], averaged over low (1986 to 1988) and high (1989-1991) solar activity periods were used to compute the average ion circulation patterns for each of the four seasons. These average circulation patterns were then compared to the average E_s morphology over Kokubunji, which was presented in Figure 10. The \vec{E} values were converted into electron drift velocities (\vec{V}_e) and plotted as hodographs, for clarity in presentation, in Figure 15. As mentioned earlier, the most dominant morphological feature is the occurrence maximum around 1000 LT (local time at 135°E longitude) in the summer. We see that \vec{V}_e at 1000 LT is in the SW quadrant during the summer and in the NW quadrant during other seasons; moreover, \vec{V}_e is found

to favor those respective quadrants ± 2 hours of 1000 LT. The initial impression then is that conditions may be favorable for E_s formation when \vec{E} (\vec{V}_e) is in the NW (SW) quadrant. Examining Figure 15(b) more closely, we see that \vec{V}_e is in the SW quadrant for most of the 24-hour day with two excursions into the SE quadrant. The periods spent in the SW quadrant are from 0400 to 1200 LT, from 1400 to 1600 LT, and 2100 to 2400 LT. In comparison, \vec{V}_e spends little time in the SW quadrant during the other seasons while spending a significant amount of the daytime hours in the NW quadrant. Finally, \vec{V}_e spends its evening and premidnight hours in the SE quadrant in all seasons.

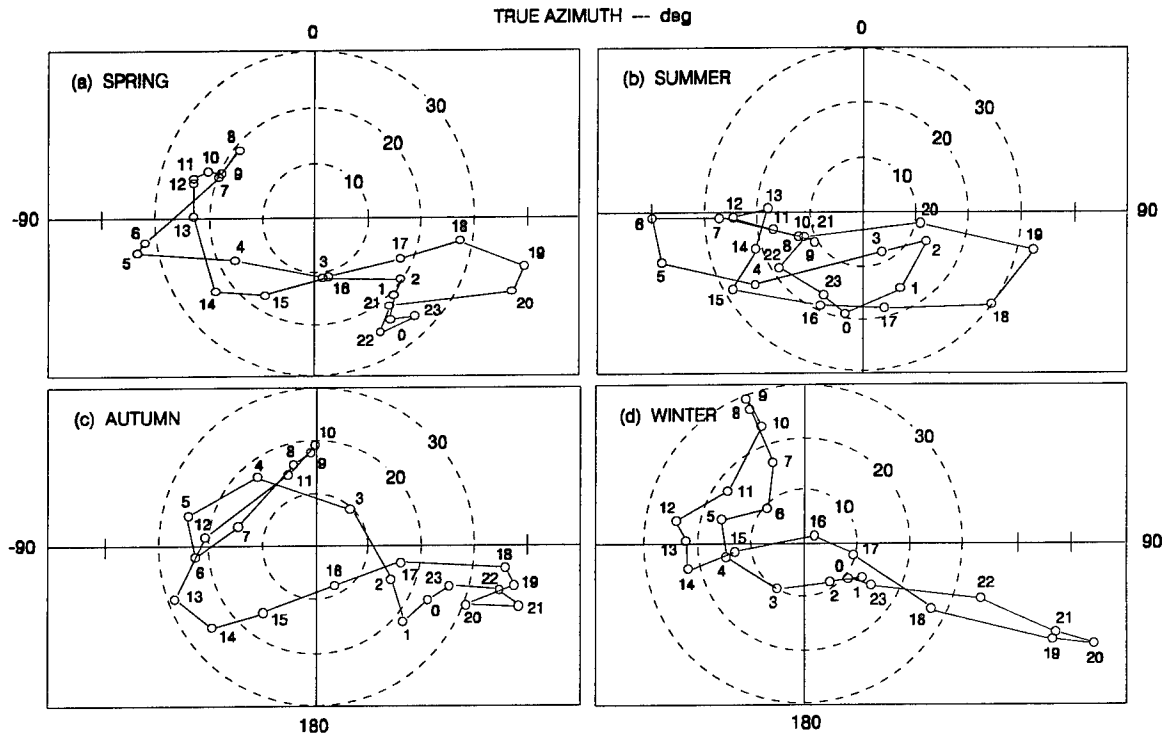


Figure 15 Hodographs of electron velocity for (a) spring, (b) summer, (c) autumn, and (d) winter over Japan under averaged solar-activity conditions.

To quantify the implications of the above \vec{V}_e patterns, we used the ion velocity equations in Section 3.3 together with the \vec{E} results presented in Figure 15 to trace ion trajectories in altitude as a function of LT. To keep the analysis simple, we inserted a distribution of ions in altitude at a specified time and then tracked the altitude of each ion as a function of LT for 24 hours. In most cases, the distribution was uniform in altitude from 100 to 145 km. Ions were placed at altitudes as low as 90 km when \vec{E} was found to exert a strong upward force on the ions. We did so to test the capability of \vec{E} to extract

ions out of the meteor source region. We assume here that the ions are distributed widely in a geographic sense such that it is only vertical transport that is important.

Ion trajectories produced by the summer \vec{E} pattern are presented in Figure 16. In Figure 16(a), the initial ion distribution was inserted at local midnight (0000 LT). With \vec{V}_e directed only slightly west of south, ion flow was convergent with weak upward motion at lower altitudes and stronger downward motion at higher altitudes. When \vec{V}_e entered the SE quadrant from 0100 LT until 0300 LT, ion motion was generally downward at all altitudes. \vec{V}_e rotated back into the SW quadrant, becoming large in magnitude and turning westward by 0600 LT. The westward directed \vec{V}_e was responsible for the strong uplifting of the ions seen around this time in Figure 16(a). Ions located initially in altitude as low as 98 km were also swept upward into the upper E and lower F regions. The maximum altitude attained by the ions was about 185 km at around 0730 LT.

The ion trajectories from 0800 to 1100 LT are of particular interest because this period corresponds to the time of maximum E_s occurrence found in Figures 10 and 11. Interestingly, \vec{V}_e was directed in a SW direction during this period which resulted once again in a downward ion motion and convergence of the injected ions into a single metallic ion layer. Downward ion transport was from 180 to 144 km in altitude during the interval, 0800 to 1000 LT; the descent rate of the ion layer was 0.3 km/min (or 5 m/s). This descending layer is reminiscent of those that have been attributed to wind shears associated with tidal modes [Fujitaka and Tohmatsu, 1973]. The ion layer in our simulation is, however, produced solely by a properly directed \vec{E} , i.e., one in the NW quadrant. Once the ion layer reaches the upper E region, it should be available for capture by a tidal wind-shear region, which would lead to further ion convergence and continued downward transport into the lower E region.

The second upward ion motion occurred when \vec{V}_e rotated CW by no more than 10° , becoming westward between 1100 and 1300 LT. The ion layer reached its second maximum in altitude (190 km) at 1400 LT before descending again when \vec{V}_e again returned to the SW quadrant. This second downward descent occurred in the afternoon and continued until 2100 LT. During the afternoon, we see that ions from altitudes as low as 90 km were brought up to participate in the circulation. What is interesting here is that this second descent of the ion layer also corresponds reasonably well with the

secondary maximum in E_s occurrence around 1800 LT found in Figure 11. From 2000 to 2400 LT, the ion layer hovered between 96 and 100 km altitude. When we allowed the ion layer to be transported by the same \vec{V}_e pattern for another 24 hours, the ion layer followed a circulation pattern similar to that shown in Figure 16(a). We have thus found that ions injected at local midnight, in the presence of the summer \vec{E} pattern, follow a stable and repeatable circulation pattern which is consistent with the times of E_s occurrence maxima.

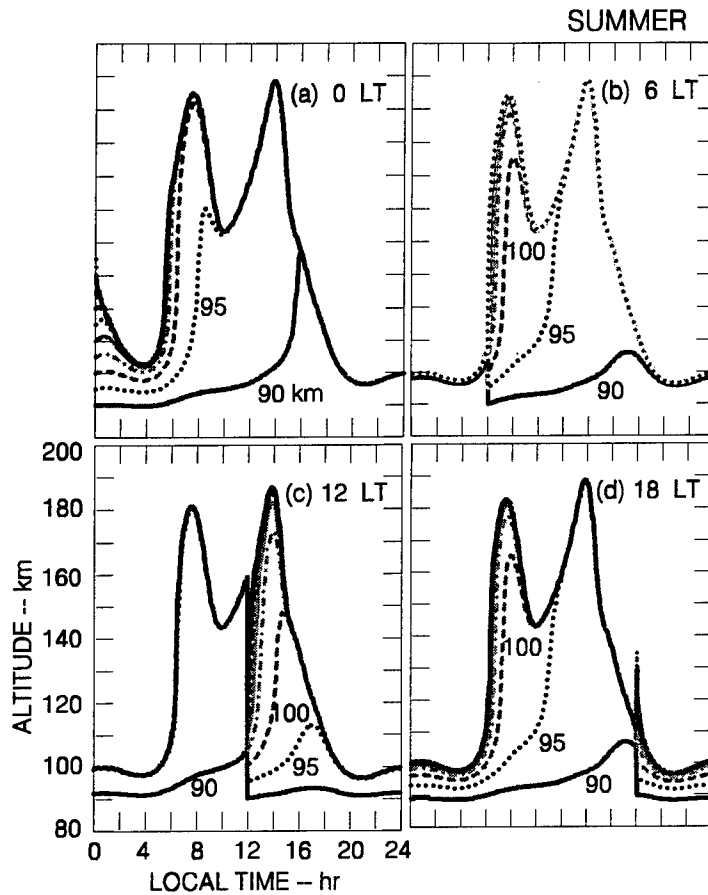


Figure 16 Trajectories of ions in altitude as a function of local time for summer conditions. Each panel is labeled by the start time of the initial ion distribution in altitude.

We ran three other sets of ion trajectories with uniform ion injections at 0600, 1200, and 1800 LT to determine whether the ion circulation pattern is sensitive to the time of ion injection or not. The ion trajectories for these cases are shown in Figures 16(b), 16(c), and 16(d). Remarkably, the circulation patterns were all similar and stable

regardless of the times of ion injection. The circulation patterns were stable enough in all cases to repeat the second day. The ion trajectories reproduced the two descending ion layers, one in the morning and the other in the late afternoon or early evening.

Ion trajectories produced by the winter \bar{E} pattern are presented in Figure 17. The patterns are seen to differ in two distinct ways from those in Figure 16. First, we note that the altitude scales in the top two panels of Figure 17 are a factor of 7 larger than

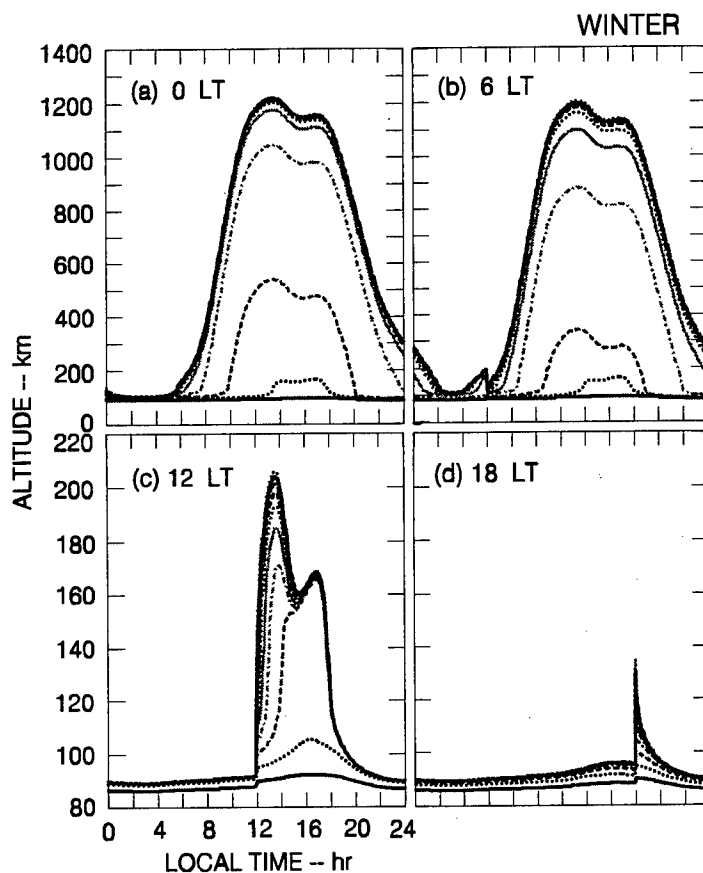


Figure 17 Ion trajectories as a function of altitude and local time during Winter conditions.

those in Figure 16, extending up to 1400 km in altitude. The larger scale, needed to display the entire trajectories followed by the ions during the course of the day, immediately indicates that upward ion transport is stronger or more sustained in time during the winter than the summer. A consequence is that the two peaks seen in Figure 16 are not seen in Figure 17. And second, the circulation patterns are not as stable nor repeatable and depend on the time of ion injection. For example, the altitude scales in the

bottom two panels are comparable to those in Figure 16 and the circulation patterns differ from those in the upper two panels. These features are described in more detail below.

The ion trajectories produced by the winter \vec{V}_e pattern when ions are injected at 0000 and 0600 LT are shown in Figures 17(a) and 17(b). The patterns are seen to be similar; the only difference is that some of the ions injected at lower altitudes at 0600 LT do not reach as high an altitude as the corresponding ions injected at local midnight. The basic pattern then is one in which metallic ions are taken out of the E region to very high altitudes during the day and premidnight periods. The ions injected at local midnight are transported downward initially by a SE-directed \vec{V}_e , but as \vec{V}_e turns westward, the ions begin to move upward in altitude (around 0400 LT). The strong upward transport of ions seen in the morning hours results from the large northward component of \vec{V}_e that can be seen in Figure 15(d) to develop, maximizing around 0900 LT. We note that this strong updrafting is produced by the upward component of the $\vec{E} \times \vec{B}$ plasma drift rather than by Pedersen ion drift.

We should also note that ions that are transported to such high altitudes are also transported poleward to comparable distances and, therefore, must be subjected to different \vec{E} patterns. Whether these ions return to the mid-latitude region has not been investigated. But we can conclude that metallic ions found in the E and lower F regions between local midnight and sunrise are ejected by the large eastward \vec{E} and, therefore, are not available for E_s formation during the day. (It is interesting to note also that ions from the meteoric deposition altitudes are transported upward into the E region. For example, ions at 94 km located around 0400 LT moved gradually upward in altitude reaching 100 km at 1100 LT, 7 hours later, and then are rapidly transported up to 160 km by 1400 LT. On the other hand, the lack of correlation between meteor activity and E_s occurrence suggests that this supply is inadequate to be a factor in the seasonal pattern of E_s occurrence.) The downward ion transport which commences after 1800 LT, the time of maximum E_s occurrence, continues until 0200 LT. Its source is seen in Figure 15(d) to be a large \vec{V}_e that is directed in the SE quadrant. Downward transport, in this case, is primarily the southward component of the $\vec{E} \times \vec{B}$ plasma drift because the Pedersen ion drift is small at those high altitudes.

The ion circulation pattern is drastically different when the ions are inserted at 1200 LT [Figure 17(c)]. The ions are still transported upward from 1200 to 1300 LT but primarily through ion Pedersen drift associated with a westward directed \vec{V}_e . Because the

upward lift is weaker at these times, the ions only reach an altitude of about 200 km. The ions are seen to converge between 1400 and 1500 LT, a period when \vec{V}_e entered the SW quadrant. The ions are then transported downward and through the E region around 1800 LT. The implication here is that there should be an ion layer descending through the E layer around local sunset in the winter. On the other hand, because these ions started their downward movement from a lower apex than those at the same times in Figures 17(a) and 17(b), they are transported to much lower altitudes, i.e., below 95 km. Once deposited at such low altitudes, they cannot easily be lifted back into ionospheric circulation. This behavior can be seen in Figure 17(c) between 2200 and 1200 LT where the ions remain below 100 km altitude throughout this period. Even the strong eastward \vec{E} in the morning period is unable to lift the ions into the E region. These results seem to be consistent with the presence of a very weak preference of E_s occurrence in the early evening rather than the morning in the winter [Smith, 1957]. The downward removal of metallic ions from the ionosphere is even more evident in Figure 17(d) where we have inserted the initial ion distribution at 1800 LT. These ions were immediately transported downward and out of ionospheric circulation.

To summarize, the winter conditions are clearly not conducive for E_s formation because of two factors: the strong eastward \vec{E} that drives most of the existing metallic ions out of the E region in the morning hours and strong SW-directed \vec{V}_e that drives the metallic ions downward and out of ionospheric circulation

The ion trajectories for spring conditions, shown in Figure 18, are seen to resemble those for winter conditions. When the ions are injected at 0000 or 0600 LT, they are transported upward to altitudes above the F layer during the day and return to the E region around 1800 LT. As in the winter, these ions are not available for E_s formation during the day. The initial trajectories are initially downward, reaching a minimum altitude just before 0400 LT; they then turn steeply upward around 0600 LT. The upward transport is not as rapid as during winter conditions because the eastward component of \vec{E} is not nearly as strong. The upward motion is produced by both $\vec{E} \times \vec{B}$ and ion Pedersen motions. The ions reach a maximum altitude around 700 km just before 1400 LT. The ion trajectories turn downward but the ions do not reach E -region altitudes until after 1900 LT. Similar trajectories are obtained when the ions are initially deposited at 0600 LT.

Ion injection at 1200 LT (Figure 18(c)) results in a rapid lifting of these ions to altitudes corresponding to the *F*-region ionosphere; again the ions are not transported to extreme altitudes. In this case, the ions reach altitudes of 200 to 240 km. With the change in \vec{E} , the ions descend and converge, reaching the *E* region around 1500 LT. The ions appear to have converged to form an ion layer as it passes through the *E* layer to lower altitudes until 1900 LT. Again, the downward transport is strong enough to force the ions out of ionospheric circulation, as indicated by the ion trajectories from 2200 to 1200 LT. The injection of ions at 1800 LT produces trajectories not unlike that shown in Figure 17, i.e., most of the ions leave the ionospheric circulation pattern. Some, however, do remain in the *E* layer during the afternoon and could take part in E_s formation. We, therefore, find that metallic ions are not readily available during the spring.

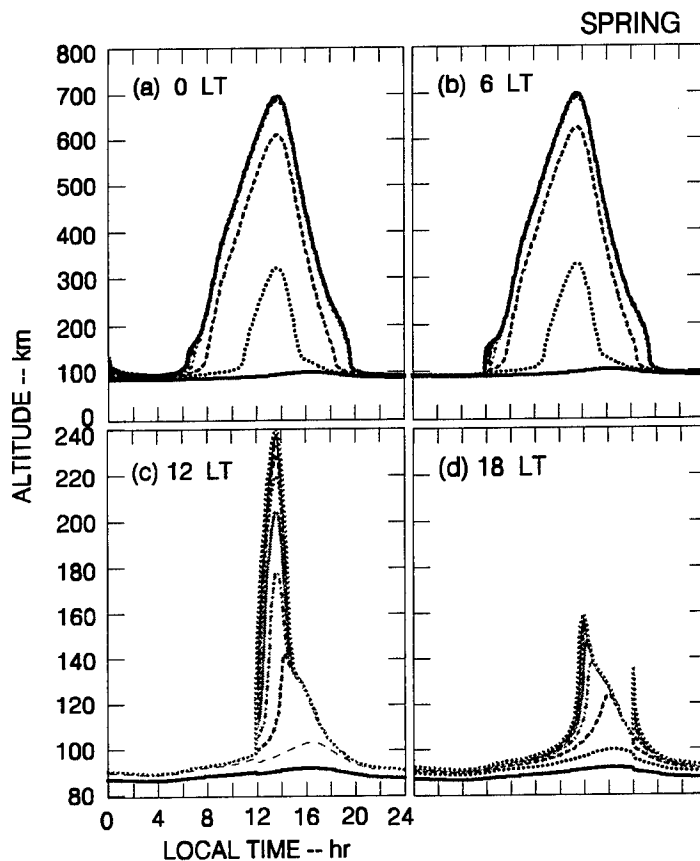


Figure 18 Ion trajectories as a function of altitude and local time for spring conditions.

Finally, the ion trajectories for autumn conditions are presented in Figure 19. The pattern is very similar to those found for the winter and spring conditions. There is a

strong upward lift around sunrise that keeps ions from being accessible for E_s formation during the day. The ions are then transported downward to E -region altitudes around sunset. But, again, ions that are deposited in the E region during the day are taken out of ionospheric circulation in the afternoon sector.

From these simulations of ion circulation, we found that only the pattern found in the summer allows the presence of metallic ions in the E region during the day. This pattern is found to be stable and repeatable regardless of when ions are deposited. In stark contrast, the circulation patterns during the other three seasons do not allow buildup of metallic ions in the E region during the day. Moreover, the patterns are not repeatable, varying with the time of ion deposition. Moreover, the patterns are such that ions are taken out of ionospheric circulation by the strong down ion transport in the afternoon.

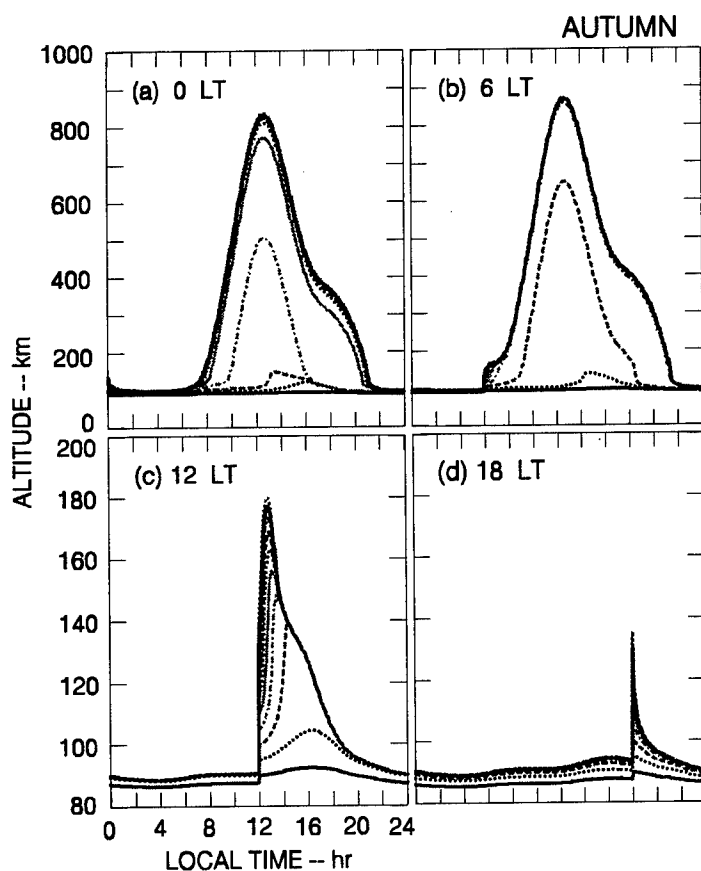


Figure 19 Ion trajectories as a function of altitude and local time for autumn conditions.

3.4.2 Solar Activity Dependence

Having demonstrated that the summer ion-circulation pattern is the only pattern capable of providing metallic ions for E_S formation, we proceed to show that this circulation pattern persists regardless of solar activity. This persistence would be consistent with the results of *Kasuya* [1958], presented in Figure 12, who showed that E_S occurrence is also independent of solar activity. Using the results from *Oliver et al.* [1993], we present in Figure 20 the summer \vec{V}_e characteristics for high and low solar activity conditions. If we compare these circulation patterns with the average summer pattern shown in Figure 15(b), we find general similarities. In particular, \vec{V}_e is predominately in the SW quadrant in all cases. This behavior, especially during the morning sector keeps the ions from being transported to high altitudes as found in other seasons.

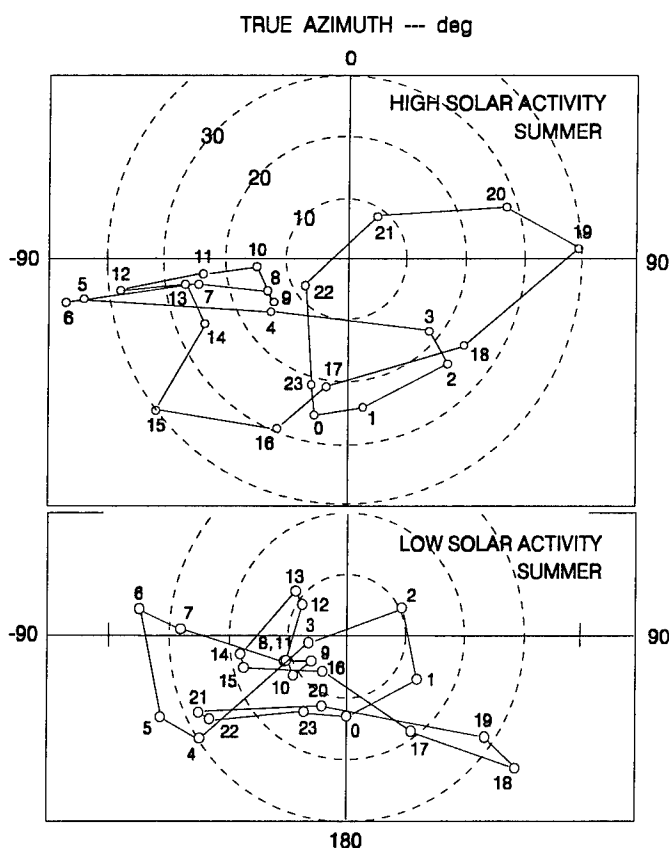


Figure 20 Hodographs of electron drift velocity as a function of local time for summer under high and low solar-activity conditions.

The ion circulation patterns for summer conditions during high solar activity are presented in Figure 21. The patterns are similar to those in Figure 16 except that the two peaks do not appear to be as developed. The source of this difference is the earlier reversal in vertical ion transport that occurs during high solar-activity conditions. The ions are seen to converge during the period 0000 to 0400 LT and then to move upward as a thick ion layer. Because of the early reversal, the ion layer reached an altitude of 160 km or less. (Note that the ordinate scale differs in Figure 21 from that in Figure 16.) The ensuing downward motion brings the ion layer down to about 140 km altitude, which is comparable to the minimum altitude reached by the ion layer under averaged solar-activity conditions. The second maximum in altitude is also not as developed as before, reaching no higher than 170 km. The upshot is that metallic ions are again available during the day for E_S formation. As we change the times of ion injection, we see that the basic circulation pattern persists as it did under averaged conditions.

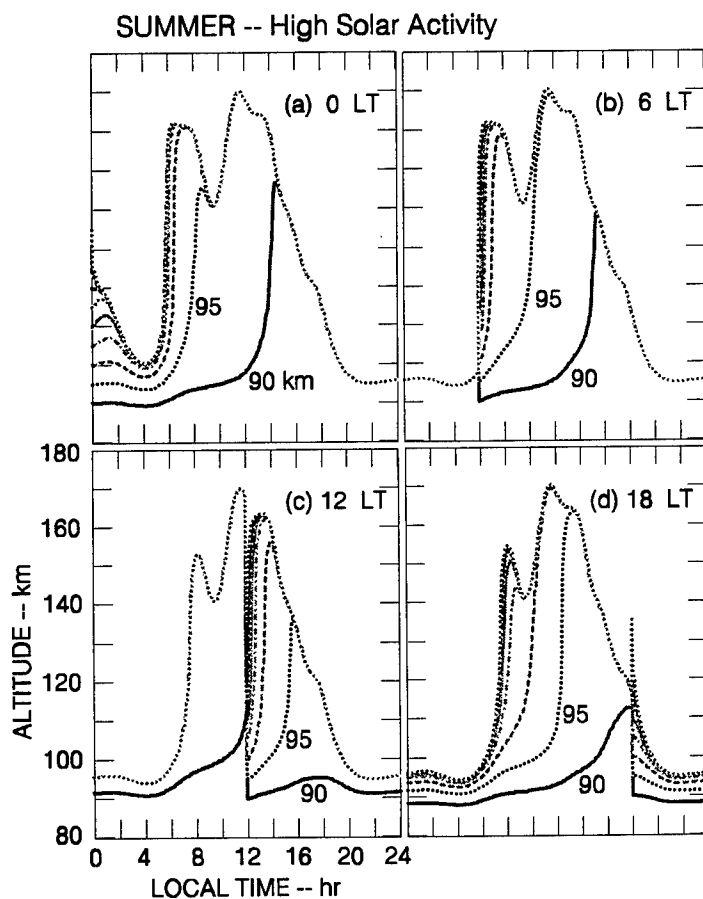


Figure 21 Circulation of metallic ions as a function of altitude and local time produced by the summer electric-field pattern under high solar-activity conditions.

The ion circulation patterns for summer conditions during low solar-activity periods are presented in Figure 22. These patterns resemble closely the patterns in Figure 16. We see pronounced double peaks, one in the morning and the other in the late afternoon. The difference between the patterns obtained for high and low solar-activity is that higher altitudes are reached under low solar activity conditions, but downward transport is such that the minimum altitude reached between the two maxima is always around 140 km. This mid-morning minimum is the feature that we describe as the metallic ion supply. The evening descent directly into the E region indicates that this ion layer could be produced entirely by \bar{E} or further compressed by wind shear. It is interesting to note, however, that the peaks have shifted to earlier times during low solar-activity conditions. Whether this shift in E_s occurrence has been reported is unclear.

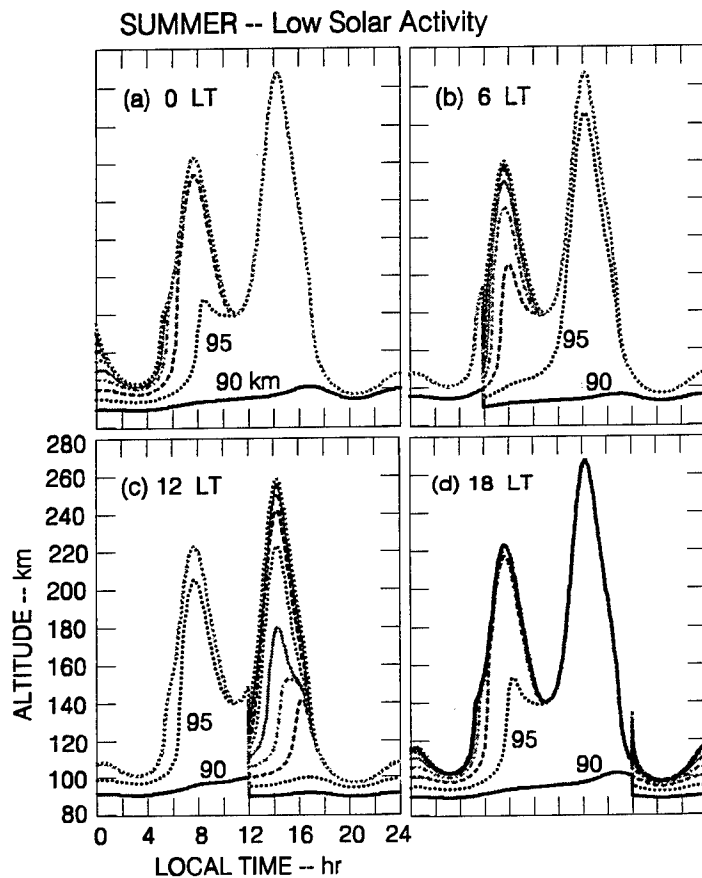


Figure 22 Circulation of metallic ions as a function of altitude and local time produced by the summer electric-field pattern under low solar-activity conditions.

Finally, we present in Figure 23 the \vec{V}_e hodographs for winter conditions during high and low solar activity. As with those from the summer, we find that the patterns persist from low to high solar activity and continue to resemble that for the averaged conditions, presented in Figure 15. Without presenting the ion-circulation patterns, we can see from Figure 23 that the features responsible for the upward ion transport to high altitudes during the day and strong downward transport around sunset persist under both conditions.

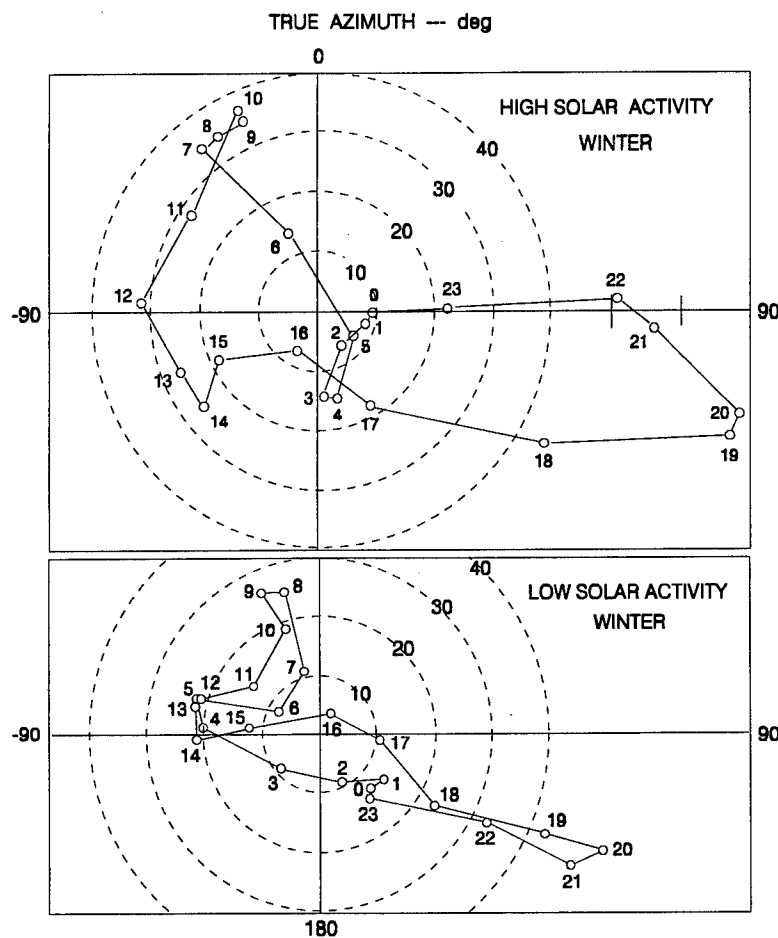


Figure 23 Hodographs of electron drift velocity as a function of local time for winter under high and low solar-activity conditions.

3.5 DISCUSSION AND CONCLUSIONS

We have shown that the diurnal variation in the direction of \vec{E} controls the circulation of metallic ions in altitude as a function of LT. And, in turn, seasonal changes

in the diurnal \vec{E} pattern determine the seasonal availability of metallic ions in the upper E region. The direction of \vec{E} turns out to be important not only because it cycles metallic ions in altitude in a diurnally favorable manner but because it acts to scavenge and gather ions toward a common altitude region. That is, when \vec{E} is in the NW quadrant, ions at low altitudes are transported upward while ions at high altitudes are transported downward. This ion convergence produced by \vec{E} appears strong enough by itself to form an E_s layer that could remain intact during its diurnal circulation. These ready-formed E_s layers were transported downward in altitude and merged with a wind-shear node once in the mid-morning and again around sunset or early evening, a pattern consistent with E_s occurrence morphology over Japan. The fact that these \vec{E} -produced E_s layers descend from about 180 km altitude suggests that they may correspond with the descending layers observed most clearly with the Arecibo incoherent-scatter radar [e.g., *Shen et al.*, 1976]. Descending layers, for the most part, have been attributed to wind-shears associated with tidal wind modes [e.g., *Fujitaka and Tohmatsu*, 1973].

The excellent correlation in the diurnal time of arrival of the metallic ion supply to E -region altitudes and E_s occurrence and the repeatability of this pattern seasonally and its independence from solar activity suggests that E_s occurrence can potentially be predicted on a shorter term basis if we are able to monitor \vec{E} .

4 DISCUSSION AND FUTURE DIRECTION

4.1 SPREAD-DOPPLER CLUTTER FROM SPORADIC- E

We have identified a new component of what has categorically been called spread-Doppler clutter. Other forms of spread-Doppler clutter have included equatorial and polar components, and meteor scatter. This new form of clutter originates as scatter from FAI imbedded in E_s layers at mid-latitudes during the night. This E_s -related phenomenon appears discrete in range but has a broad Doppler spectrum. These discrete echoes can appear as false targets that persist for several minutes while moving inward toward the radar. Unlike meteor echoes, however, the spectral broadening does not result from an impulsive temporal behavior. Instead, we have developed an altitude-modulated E_s model for a new polarization process that results in an enhanced \vec{E} . If this newly discovered polarization model is shown to be realistic, it will impact our interpretation of propagation effects that can occur at mid-latitudes. We would no longer be able to bound spectral broadening in terms of ambient \vec{E} values. Altitude-modulated E_s layers would also provide a means of supporting micro-multipaths.

Before we can model this new form of clutter, a number of tasks remain. There is need to determine the strength of this clutter and compare it to other forms of clutter. There is also need to estimate the frequency band over which it can operate. While the results (Section 2) were obtained from radar measurements at 46.5 MHz, there is published evidence that this form of backscatter is observed as low as 16 MHz. Thus far, there is no experimental evidence for this form of clutter at frequencies below 16 MHz. We are still uncertain about the details of the polarization process and the extent to which that process is needed to produce any backscatter.

4.2 SPORADIC- E MODELING

We have shown for the first time that the ionospheric electric field determines the seasonal behavior of E_s occurrence by controlling the availability of metallic ions in the E region. The agreement between the times of metallic-ion availability and the statistical occurrence of E_s is striking for the measurements made in Japan. It would be desirable to determine how well this relationship is maintained for other geographic locations. Having identified a physical parameter that is associated with E_s appearance in a

statistical sense, the next step is to consider how we can use this information to develop a predictive model for E_s . Considerable work remains to be done. We need to have a better idea of where new metallic ions are injected into the ionosphere. One approach is to construct a model that includes meteoric deposition of neutral metallic atoms and solar ionization and charge exchange processes that produce metallic ions. This model can then be combined with the electric field circulation model to account for the availability of metallic ions. Finally, a tidal wind system can be included to account for wind shear production of E_s layers.

4.3 FUTURE DIRECTION

During the second half of this project period, we will be spending considerable effort on the problem of equatorial spread-Doppler clutter. As already mentioned, spread-Doppler clutter is perhaps the most serious of obstacles to effective OTHR performance. It is the least understood of OTHR problems, having being discovered fairly recently, and perhaps the most visible in the OTHR community. A considerable amount of effort is being devoted to this subject. It is a central issue being considered together by the United States and Australia under the joint U.S - Australian Memorandum of Understanding. We are in the process of considering what can be done experimentally and from a modeling point of view to address this problem.

REFERENCES

- Axford, W. I., Note on a mechanism for the vertical transport of ionization in the ionosphere, *Can. J. Phys.*, 39, 1393, 1961.
- Basu, S., R. L. Vesprini, and J. Aarons, Field-aligned ionospheric *E*-region irregularities and sporadic *E*., *Radio Sci.*, 8, 235, 1973.
- Behnke, R., and T. Hagfors, Evidence for the existence of nighttime *F*-region polarization fields at Arecibo, *Radio Sci.*, 9, 211, 1974.
- Behnke, R., and J. Vickrey, Radar evidence for Fe^+ in a sporadic-*E* layer, *Radio Sci.*, 10, 325, 1975.
- Burnside, R. G., J. C. G. Walker, R. A. Behnke, and C. A. Gonzales, Polarization electric fields in the nighttime *F* layer at Arecibo, *J. Geophys. Res.*, 88, 6259, 1983.
- Chimonas, G., and W. I. Axford, Vertical movement of temperate-zone sporadic-*E* layers, *J. Geophys. Res.*, 73, 111, 1968.
- Chiu, Y. T., and J. M. Straus, Rayleigh-Taylor and wind-driven instabilities of the nighttime equatorial ionosphere, *J. Geophys. Res.*, 84, 3283, 1979.
- Ellyett, C.D., and P.F. Goldsbrough, Relationship of Meteors to Sporadic E 1. A Sorting of Facts, *J. Geophys. Res.*, 81, 6131, 1976.
- Ecklund, W. L., D. A. Carter, and B. B. Balsley, Gradient-drift irregularities in mid-latitude sporadic-*E*, *J. Geophys. Res.*, 86, 858, 1981.
- Farley, D. T., A theory of electrostatic fields in the ionosphere at nonpolar geomagnetic latitudes, *J. Geophys. Res.*, 65, 869, 1960.
- Farley, D. T., and B. B. Balsley, Instabilities in the equatorial electrojet, *J. Geophys. Res.*, 78, 227, 1973.
- Fejer, B. G., J. Providakes, and D. T. Farley, Theory of plasma waves in the auroral *E* region, *J. Geophys. Res.*, 89, 7487, 1984.
- From, W. R., Sporadic *E* movement followed with a pencil beam high frequency radar, *Planet. Space Sci.*, 31, 1397, 1983.
- Fujitaka, K., and T. Tohmatsu, A tidal theory of the ionospheric intermediate layer, *J. Atmos. Terr. Phys.*, 35, 425, 1973.
- Fukao, S., M. C. Kelley, T. Shirakawa, T. Takami, M. Yamamoto, T. Tsuda, and S. Kato, Turbulent upwelling of the mid-latitude ionosphere, 1. Observational results by the MU radar, *J. Geophys. Res.*, 96, 3725, 1991a.

- Fukao, S., W. L. Oliver, Y. Onishi, T. Takami, T. Sato, T. Tsuda, M. Yamamoto, and S. Kato, *F*-region seasonal behavior as measured by the MU radar, *J. Atmos. Terr. Phys.*, 53, 599, 1991b.
- Goodwin, G. L., Some aspects of direct backscatter echoes from sporadic-*E*, *J. Atmos. Terr. Phys.*, 11, 177, 1965.
- Goodwin, G. L., and J. A. Thomas, Field-aligned irregularities in the *E_s* region, *J. Atmos. Terr. Phys.*, 25, 707, 1963.
- Grebowsky, J. M., and M. W. Pharo III, The source of midlatitude metallic ions at *F*-region altitudes, *Planet. Space Sci.*, 33, 807, 1985.
- Greenwald, R. A., Diffuse radar aurora and the gradient drift instability, *J. Geophys. Res.*, 79, 4807, 1974.
- Hanson, W. B., and S. Sanatani, Meteoric ions above the *F₂* peak, *J. Geophys. Res.*, 75, 5503, 1970.
- Hanson, W. B., D. L. Sterling, and R. F. Woodman, Source and identification of heavy ions in the equatorial *F* layer, *J. Geophys. Res.*, 77, 5530, 1972.
- Harper, R. M., and J. C. G. Walker, Comparison of electrical conductivities in the *E*- and *F*-regions of the nocturnal ionosphere, *Planet. Space Sci.*, 25, 197, 1977.
- Harper, R. M., R. H. Wand, and J. D. Whitehead, Comparison of Arecibo *E*-region data and sporadic-*E* theory: A measurement of the diffusion coefficient, *Radio Sci.*, 10, 357, 1975.
- Hedberg, Ake, Seasonal Variations in the Correlation of Meteors and Sporadic *E*, *J. Atmos. Terr. Phys.*, 38, 785, 1976.
- Hines, C. O., Internal atmospheric gravity waves at ionospheric heights, *Can. J. Phys.*, 38, 1441, 1960.
- Hines C.O., Prevailing and tidal wind shears in the *E* region, *Radio Sci.*, 1, 169, 1966.
- Itoh, T., M. Nakamura, and Y. Nakamura, Rocket observation of electron density irregularities in the middle latitude *E* region, *Geophys. Res. Lett.*, 2, 553, 1975.
- Jacchia, L. G., Revised static models of the thermosphere and exosphere with empirical temperature profiles, *Spec. Rept. 332*, Smithsonian Astrophys. Observ., Cambridge, Massachusetts, 1971.
- Kasuya, I., Long term variations of the sporadic *E* layer in Japan, *J. Radio Res. Lab. Japan*, 5, 117, 1958.
- Kato, S., Cross-field instability for the formation of sporadic-*E*, *Radio Sci.*, 7, 417, 1972.
- Keys, J. G., and M. K. Andrews, Gravity wave and sporadic-*E* echo signatures on VHF backscatter radar systems, *Planet. Space Sci.*, 32, 1455, 1984.

- Koren'kov, Yu. N., Effect of motions in the neutral atmosphere on the seasonal-daily behavior of the E_s layer, *Geomag. Aeron.*, 19, 15, 1979.
- Koren'kov, Yu. N., and M. G. Deminov, Redistribution of electron density in the E region of the mid-latitude ionosphere under the effect of a stationary homogeneous wind system, *Geomag. Aeron.*, 20, 296, 1980.
- Kudeki, E., D. T. Farley, and B. G. Fejer, Long wavelength irregularities in the equatorial electrojet, *Geophys. Res. Lett.*, 9, 684, 1982.
- Kumar, S., and W. B. Hanson, The morphology of metallic ions in the upper atmosphere, *J. Geophys. Res.*, 85, 6783, 1980.
- Lanchester, B. S., T. Nygren, A. Huuskonen, T. Turunen, and M. J. Jarvis, Sporadic- E as a tracer for atmospheric waves, *Planet. Space Sci.*, 39, 1421, 1991.
- MacDougall, J. W., 110 km neutral zonal wind patterns, *Planet. Space Sci.*, 22, 545, 1974.
- MacDougall, J. W., Seasonal variation of semidiurnal winds in the dynamo region, *Planet. Space Sci.*, 26, 705, 1978.
- MacLeod, M. A., Sporadic E theory. I. Collision-geomagnetic equilibrium, *J. Atmos. Sci.*, 23, 96, 1966.
- MacLeod, M.A., T. Keneshea, and R. Narcisi, Numerical modelling of a metallic ion sporadic- E -layer, *Radio Sci.*, 10, 371, 1975.
- Maeda, K., T. Tsuda, and H. Maeda, Theoretical interpretation of the equatorial sporadic E layers, *Rep. Ionos. Space Res. Jap.*, 17, 3, 1963.
- Mende, S. B., G. R. Swenson, and K. L. Miller, Observations of E and F region Mg^+ from Spacelab 1, *J. Geophys. Res.*, 90, 6667, 1985.
- Miller, K. L., and L. G. Smith, Incoherent scatter radar observations of irregular structure in mid-latitude sporadic- E layers, *J. Geophys. Res.*, 83, 3761, 1978.
- Narcisi, R. S., Processes associated with metal-ion layers in the E region of the ionosphere, *Space Res.*, 8, 360, 1968.
- Nygren, T., L. Jalonen, J. Oksman, and T. Turunen, The role of electric field and neutral wind direction in the formation of sporadic E -layers, *J. Atmos. Terr. Phys.*, 46, 373, 1984.
- Oliver, W. L., Y. Yamamoto, T. Takami, S. Fukao, M. Yamamoto, and T. Tsuda, MU radar observations of ionospheric electric fields, *J. Geophys. Res.*, 98, 11,615, 1993.
- Rees, D., E. B. Dorling, K. H. Lloyd, and C. Low, The role of neutral winds and ionospheric electric field in forming stable sporadic E -layers, *Planet. Space Sci.*, 24, 475, 1976.
- Riggin, D., and A. Kadish, Nonlocal theory of long-wavelength plasma waves associated with sporadic- E layers, *J. Geophys. Res.*, 94, 1495, 1989.

- Riggin, D., W. E. Swartz, J. Providakes, and D. T. Farley, Radar studies of long-wavelength waves associated with mid-latitude sporadic- E layers, *J. Geophys. Res.*, **91**, 8011, 1986.
- Rishbeth, H., The F -layer dynamo, *Planet. Space Sci.*, **19**, 263, 1971.
- Rowe, J. F., Downward transport of nighttime E_s -layers into the lower E -region at Arecibo, *J. Geophys. Res.*, **36**, 225, 1974.
- Rowe, J. F., and G.F. Gieraltowski, Ion layer formation by uniform neutral winds in the nighttime E region, *J. Geophys. Res.*, **79**, 2917, 1974.
- Sagalyn, R. C., M. Smiddy, and W. P. Sullivan, Experimental investigation of the nighttime E region, *Space Res.*, **7**, 448, 1967.
- Shen, J. S., W.E. Swartz, and Donald T. Farley, Ionization Layers in the Nighttime E Region Valley Above Arecibo, *J. Geophys. Res.*, **81**, 5517 - 5526, 1976.
- Simon, A., Instability of a partially ionized plasma in crossed electric and magnetic fields, *Phys. Fluids*, **6**, 382, 1963.
- Sinno, K., C. Ouchi, and C. Nemoto, Structure and movement of E_s detected by LORAN observations, *J. Radio Res. Japan*, **11**, 45, 1964.
- Sinno, K.C., M. Kan, and Y. Hirukawa, On the Reflection and Transmission Losses for Ionospheric Radio Wave Propagation Via Sporadic E , *J. Radio Res. Japan*, **110**, 65-84, 1976.
- Smith, E. K., Worldwide Occurrence of Sporadic E , *National Bureau of Standards Circular 582*, 1957.
- Smith, E. K., Some unexplained features in the statistics for intense sporadic E , in *Second Seminar on the Cause and Structure of Temperate Latitude Sporadic E*, Paper 12, Vail, Colorado, 1968.
- Smith, Georgellen, and V.E. Hatfield, AMBCOM User's Guide for Engineers, SRI International, 1987
- Smith, L. G., Rocket observations of sporadic E and related features of the E region, *Radio Sci.*, **1**, 178, 1966.
- Smith, L. G., A sequence of rocket observations of night-time sporadic- E , *J. Atmos. Terr. Phys.*, **32**, 1247, 1970.
- Smith, L. G., and E. A. Mechtly, Rocket observations of sporadic- E layers, *Radio Sci.*, **7**, 367, 1972.
- Smith, L. G., and K. L. Miller, Sporadic- E and unstable wind shears, *J. Atmos. Terr. Phys.*, **42**, 45, 1980.
- Sudan, R. N., J. Akinrimisi, and D. T. Farley, Generation of small-scale irregularities in the equatorial electrojet, *J. Geophys. Res.*, **78**, 240, 1973.

- Swider, W., Ionic and neutral concentrations of Mg and Fe near 92 km, *Planet. Space Sci.*, 32, 307, 1984.
- Tanaka, T., and S. V. Venkateswaran, Characteristics of field-aligned *E*-region irregularities over Iioka (36°N), Japan -- I, *J. Atmos. Terr. Phys.*, 44, 381, 1982a.
- Tanaka, T., and S. V. Venkateswaran, Characteristics of field-aligned *E*-region irregularities over Iioka (36°N), Japan -- II, *J. Atmos. Terr. Phys.*, 44, 395, 1982b.
- Triskova, L., On the seasonal variation in the temperate Es occurrence, *J. Atmos. Terr. Phys.*, 36, 861-869, 1974.
- Tsuda, T., T. Sato, and K. Maeda, Formation of sporadic-*E* layers at temperate latitudes due to vertical gradients of charge density, *Radio Sci.*, 1, 212, 1966.
- Tsunoda, R. T., Doppler velocity maps of the diffuse radar aurora, *J. Geophys. Res.*, 81, 425, 1976.
- Tsunoda, R.T., M. Williams, and Y. Zambre, A Comprehensive *E*-Region Auroral Clutter (CERAC) Model Description, Results, and Validation, *Final Technical Report*, SRI International, Menlo Park, Ca., 1991.
- Unwin, R. S., and F. B. Knox, The morphology of the v.h.f. radio aurora at sunspot maximum -- IV, *J. Atmos. Terr. Phys.*, 30, 25, 1968.
- Vergasova, G. V., Ye. I. Zhovtyy and E. S. Kazimirovskiy, Empirical model of general atmospheric circulation at ionospheric levels above 100 km, *Geomag. Aeron.*, 17, 464, 1977.
- Whitehead, J. D., The formation of the sporadic-*E* layer in the temperate zones, *J. Atmos. Terr. Phys.*, 20, 49-58, 1961.
- Whitehead, J. D., Production and prediction of sporadic *E*, *Rev. Geophys. Space Phys.*, 8, 65, 1970.
- Whitehead, J. D., Ionization disturbances caused by gravity waves in the presence of an electrostatic field and background wind, *J. Geophys. Res.*, 76, 238, 1971.
- Whitehead, J. D., Winds in the *E* region, *Radio Sci.*, 7, 403, 1972.
- Whitehead, J. D., Recent work on mid-latitude and equatorial sporadic-*E*, *J. Atmos. Terr. Phys.*, 51, 401-424, 1989.
- Woodman, R. F., M. Yamamoto, and S. Fukao, Gravity wave modulation of gradient drift instabilities in mid-latitude sporadic *E* irregularities, *Geophys. Res. Lett.*, 18, 1197, 1991.
- Yamamoto, M., S. Fukao, R. F. Woodman, T. Ogawa, T. Tsuda, and S. Kato, Mid-latitude *E* region field-aligned irregularities observed with the MU radar, *J. Geophys. Res.*, 96, 15,943, 1991.

Yamamoto, M., S. Fukao, T. Ogawa, T. Tsuda, and S. Kato, A morphological study on mid-latitude *E*-region field-aligned irregularities observed with the MU radar, *J. Atmos. Terr. Phys.*, 54, 769, 1992.

Yamamoto, M., N. Komoda, S. Fukao, R. T. Tsunoda, T. Ogawa, and T. Tsuda, Spatial structure of the *E*-region field-aligned irregularities revealed by the MU radar, *Radio Sci.*, in press, 1993.